

## Study of phase-separation dynamics by use of cell dynamical systems. I. Modeling

Y. Oono and S. Puri

*Department of Physics and Materials Research Laboratory, 1110 W. Green Street,  
University of Illinois at Urbana-Champaign, Urbana, Illinois 61801*

(Received 17 July 1987)

We present a computationally efficient scheme of modeling the phase-ordering dynamics of thermodynamically unstable phases. The scheme utilizes space-time discrete dynamical systems, viz., cell dynamical systems (CDS). Our proposal is tantamount to proposing new *Ansätze* for the kinetic-level description of the dynamics. Our present exposition consists of two parts: part I (this paper) deals mainly with methodology and part II [S. Puri and Y. Oono, Phys. Rev. A (to be published)] gives detailed demonstrations. In this paper we provide a detailed exposition of model construction, structural stability of constructed models (i.e., insensitivity to details), stability of the scheme, etc. We also consider the relationship between the CDS modeling and the conventional description in terms of partial differential equations. This leads to a new discretization scheme for semilinear parabolic equations and suggests the necessity of a branch of applied mathematics which could be called "qualitative numerical analysis."

### I. INTRODUCTION

One of the outstanding difficult problems in the study of phase transitions is the ordering dynamics of thermodynamically unstable phases, e.g., spinodal decomposition.<sup>1</sup> Many analytical<sup>2-6</sup> and numerical<sup>7-10</sup> approaches have been applied to this problem. Since, however, the problem of phase separation is intrinsically highly nonlinear, it can hardly be said that approximations used in analytical theories (especially for long-time behavior) are well controlled. Consequently, we do not know how reliable they actually are. Numerical simulations (mainly Monte Carlo simulations) are valuable. However, for a study of long-time behavior (e.g., the so-called scaling regime in spinodal decomposition), the computational limitations are still appreciable.

The present exposition consists of two parts. Part I (this paper) proposes a cell-dynamical-system approach to phase-separation dynamics and studies general features of the approach. In part II (Ref. 11) we study two-dimensional systems in detail, both without and with noise. Our main philosophy in this study is as follows: *Nature gives physicists phenomena, not equations*. Hence it is important to explore the possibility of directly describing these phenomena by computationally efficient means without considering the conventional analytical formulation in terms of partial differential equations.

A cell dynamical system (CDS) is a map  $T: A^L \rightarrow A^L$ , where  $A$  is a set and  $L$  is a lattice structure (in the physicists' sense, say, a  $d$ -cubic lattice). The set  $A$  is the totality of the local states of a single cell (e.g., up and down states of spins in the Ising model). Thus  $A^L$  is the set of all the states (configurations) of the system;  $A^L$  is the phase space. Cellular automata<sup>12(a)</sup> (CA) and coupled maps<sup>12(b),12(c)</sup> are examples of CDS's. The conventional discretization of partial differential equations gives a CDS. The CDS approach has been successfully used for some time; notable examples are those of CA hydrodynamics<sup>13(a)</sup> and magnetohydrodynamics,<sup>13(b)</sup> CA

versions of the Ising and  $XY$  models,<sup>14(a)</sup> a model of crystal growth,<sup>14(b)</sup> chemical pattern dynamics,<sup>15</sup> etc. As can be seen from these examples, there are two categories of CDS models: one is metaphorical (as in the models for chemical pattern dynamics) and the other realistic (as in the case of CA hydrodynamics). Models in the former category may be caricatures of reality, but their simplicity makes an in-depth study possible.<sup>15(b)</sup> Models in the latter category are devised mainly for computational efficiency. Because of this efficiency, they can be used to study effects which are hard to approach analytically or by conventional numerical methods. Our modeling of phase-separation kinetics is in the second category, as will be demonstrated in part II (Ref. 11).

In Sec. II, an approach whereby CDS models can be constructed is explained. This is an *ab initio* modeling with the aid of intuitive ideas about the systems. The modeling does not give a unique model for the system we wish to describe. However, there is a universality which justifies the intuitive modeling, i.e., phenomenological results of the resultant models are virtually independent of their details. Although the main body of numerical results will be presented in part II (Ref. 11), we provide representative examples in Sec. III. In Sec. IV, we discuss the relation of resultant models and the conventional modeling in terms of partial differential equations. A new discretization scheme for partial differential equations is proposed and some of its mathematical properties are discussed. In Sec. V, we end with a discussion and summary.

### II. ELEMENTARY CONSTRUCTION OF CDS MODELS

#### A. General discussion

Throughout this paper we consider systems without hydrodynamic interactions. Thus we would like to model phase-ordering kinetics in the model  $A$  (with a noncon-

served order parameter, e.g., ferromagnets) and the model  $B$  (with a conserved order parameter, e.g., binary alloys).<sup>16</sup> Our original motivation in devising computationally efficient models was the study of the model- $H$  systems (with a conserved order parameter and hydrodynamic interactions, e.g., binary fluids), which requires a large three-dimensional system because of the long-range nature of hydrodynamic interactions. This study is in progress.

In almost all analytical approaches, the starting point for a theory of phase ordering (and separation) kinetics is a stochastic partial differential equation. Model- $A$  dynamics is usually described by the time-dependent Ginzburg-Landau (TDGL) equation,

$$\frac{\partial \psi(\mathbf{r}, t)}{\partial t} = -L \frac{\delta H[\psi(\mathbf{r}, t)]}{\delta \psi(\mathbf{r}, t)} + \sigma(\mathbf{r}, t), \quad (2.1)$$

where  $\psi(\mathbf{r}, t)$  is the order parameter of the system at point  $\mathbf{r}$  at time  $t$ ;  $L$  is a phenomenological parameter;  $H[\psi(\mathbf{r}, t)]$  is usually the coarse-grained  $\phi^4$  free-energy functional;<sup>17</sup>

$$H[\psi(\mathbf{r}, t)] = \int d\mathbf{r} \left[ \frac{1}{2} (\nabla \psi)^2 - \frac{\tau}{2} \psi^2 + \frac{g}{4} \psi^4 \right], \quad (2.2)$$

with  $\tau, g$  being phenomenological parameters greater than zero. The parameter  $\tau$  measures the depth of the quench. The Gaussian white noise  $\sigma(\mathbf{r}, t)$  has the following expectation values:

$$\begin{aligned} \langle \sigma(\mathbf{r}, t) \rangle &= 0, \\ \langle \sigma(\mathbf{r}, t) \sigma(\mathbf{r}', t') \rangle &= 2L \delta(\mathbf{r} - \mathbf{r}') \delta(t - t'). \end{aligned} \quad (2.3)$$

Model- $B$  dynamics is described by the Cahn-Hilliard-Cook (CHC) equation,<sup>2</sup>

$$\frac{\partial \psi(\mathbf{r}, t)}{\partial t} = L \nabla^2 \frac{\delta H[\psi(\mathbf{r}, t)]}{\delta \psi(\mathbf{r}, t)} + \sigma(\mathbf{r}, t), \quad (2.4)$$

where symbols have the same meaning as previously. This time, the Gaussian white noise  $\sigma(\mathbf{r}, t)$  has the following expectation values:

$$\begin{aligned} \langle \sigma(\mathbf{r}, t) \rangle &= 0, \\ \langle \sigma(\mathbf{r}, t) \sigma(\mathbf{r}', t') \rangle &= -2L \nabla^2 \delta(\mathbf{r} - \mathbf{r}') \delta(t - t'). \end{aligned} \quad (2.5)$$

The deterministic (without noise) version of (2.4) is known as the Cahn-Hilliard (CH) equation. In the conserved-order-parameter case (model  $B$ ),  $\int d\mathbf{r} \psi(\mathbf{r}, t)$  is a constant. It should be noted that, strictly speaking, these equations cannot be derived from more microscopic descriptions of the systems. This is clear if we recall the ‘‘derivation’’ of the  $\phi^4$  free-energy functional from the Ising model;<sup>17</sup> formal derivation may seem possible, but, as is well known, the real-space renormalization suffers from a proliferation of higher-order terms. Thus a mathematically well-controlled truncation is impossible. At best, we should regard these partial-differential-equation models as *Ansätze* connecting the coarse-grained free energy with the coarse-grained description of phase-ordering dynamics.<sup>18(a)</sup> Actually, the Cahn-Hilliard-Cook equa-

tion may not be an adequate model of binary-alloy spinodal decomposition.<sup>5,18(b)</sup>

The spatially coarse-grained description implies coarse-graining in time also. Then, the partial-differential-equation approach need not be the only one. Rather, we can explicitly take into account the coarse-graining in time. If the resolution of the spatial structure is  $L$ , then the behavior of the model at time scales smaller than  $L^2/D$  (where  $D$  is the typical diffusion constant of the system) need not be specified exactly. In the spatially coarse-grained model it is natural to directly relate the configurations at time  $t$  and at time  $t + \Delta t$ , where  $\Delta t$  is of order  $L^2/D$ . Therefore we should model phase-ordering dynamics by a map connecting these two configurations. This type of modeling is tantamount to proposing new *Ansätze*.

### B. Intuitive modeling of phase-separation dynamics

Modeling of phase-separation dynamics consists of two steps: (1) modeling of each cell; (2) connecting cells. The first step is essentially the calculation of the driving force due to the chemical potential. Whether or not the order parameter is conserved is not a property of individual cells, but rather of the relationship between cells. Thus the conservation and other extra constraints should be considered in step (2).

We assume that the local dynamics of the system (e.g., the dynamics of an isolated cell) is governed by a relaxational mechanism driven by the local free-energy functional. The shape of the local free-energy functional is sketched in Fig. 1(a). The behavior of the order parameter observed at time intervals of  $\Delta t$  can be mimicked by an injection  $f$  of  $\mathbf{R}$  (the set of real numbers) as is shown in Fig. 1(b).<sup>19</sup> We choose this map  $f$  to describe the local

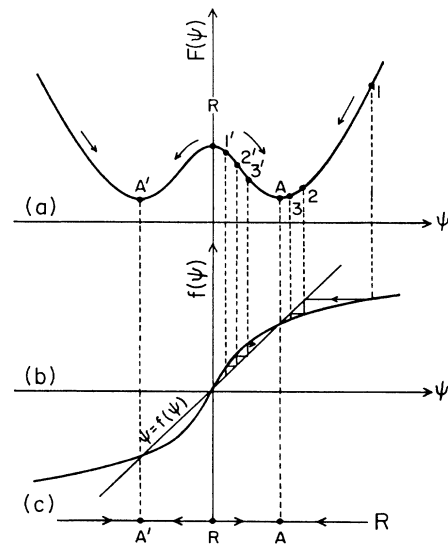


FIG. 1. (a) Coarse-grained free energy  $F$  at the scale of the correlation length. If the local order parameter takes the value at 1 ( $1'$ ), then after one time step it takes the value at 2 ( $2'$ ), etc. This motivates the injection  $f: \mathbf{R} \rightarrow \mathbf{R}$  shown in (b) which can describe the behavior. (c) The flow due to this map.  $A$  and  $A'$  are hyperbolic sinks and  $R$  is the hyperbolic source.

dynamics of each cell (without any constraints).

In Fig. 1(c) the flow due to the map  $f$  on  $\mathbf{R}$  is described. It should be realized that what we really need is this flow diagram; even though we used a local free-energy functional for a heuristic purpose in the preceding paragraph, we do not actually need the functional to construct CDS models. The important features of this flow are that there is a single hyperbolic unstable fixed point and that there are two hyperbolic stable fixed points symmetrically placed on each side of the unstable fixed point. The stable fixed points correspond to the two ordered states after quenching. The unstable fixed point corresponds to the disordered state before quenching.

There are many injections with this type of flow diagram, so that Fig. 1(c) cannot uniquely specify a map. However, we believe that any (piecewise) smooth continuous injection with one hyperbolic source and two symmetrically placed hyperbolic sinks gives similar phenomenological results. This assertion of universality is discussed in greater detail later. For the moment, let us choose a convenient map  $f$  with a flow as shown in Fig. 1(c). The

single cell dynamics is described by

$$\psi(t+1, n) = f(\psi(t, n)), \quad (2.6)$$

where  $\psi(t, n)$  is the value of the order parameter in the cell  $n$  at time  $t$ . Next we must connect cells to take into account the spatial cooperative interactions. The resultant driving force on the order parameter  $\psi(t, n)$  should be proportional to its difference from the average of the order parameters in the neighborhood cells. Thus the CDS model for the case with nonconserved order parameter reads<sup>19</sup>

$$\begin{aligned} \psi(t+1, n) &= f(\psi(t, n)) + D[\langle\langle \psi(t, n) \rangle\rangle - \psi(t, n)] \\ &\equiv \mathcal{F}[\psi(t, n)], \end{aligned} \quad (2.7)$$

where  $D$  is a positive constant proportional to the phenomenological diffusion constant;  $\langle\langle * \rangle\rangle - *$  is essentially the isotropized discrete Laplacian. We use the following definition of  $\langle\langle * \rangle\rangle$  on the two-dimensional square lattice:

$$\langle\langle \psi(t, n) \rangle\rangle = \frac{1}{6} \sum (\psi \text{ in the nearest-neighbor cells}) + \frac{1}{12} \sum (\psi \text{ in the next-nearest-neighbor cells}). \quad (2.8)$$

The inclusion of the contributions from the next-nearest-neighbor cells is not necessary in the nonconserved-order-parameter case. However, it is crucial in the conserved-order-parameter case to make the model isotropic. We see this later in Sec. III. It is easy to introduce an anisotropy effect in the conserved case by suitably modifying the definition of  $\langle\langle * \rangle\rangle$ . The net gain  $\mathcal{F}[\psi(t, n)] - \psi(t, n)$  of the center cell should be proportional to the driving force due to the chemical potential (including the gradient term).

To arrive at the model for the case with the conserved order parameter, we must impose auxiliary conditions. The conservation of the order parameter implies the local sum rule: when there is an exchange of order parameter values between a cell and its neighboring cells, there should not be a net change of the order parameter inside the neighborhood surrounding the center cell. Since the net gain of the order parameter by the center cell is given by  $\mathcal{F}[\psi(t, n)] - \psi(t, n)$ , the discrete model for the conserved case reads<sup>19</sup>

$$\psi(t+1, n) = \mathcal{F}[\psi(t, n)] - \langle\langle \mathcal{F}[\psi(t, n)] - \psi(t, n) \rangle\rangle. \quad (2.9)$$

A more intuitive explanation of our discrete model for the conserved case can be found in Fig. 2. In (2.9), the subtraction corresponds to the extra Laplacian in the CH equation.

Thus we have arrived at deterministic CDS models. The models are intrinsically computationally efficient and ideally suited to a parallel computation environment. However, we did not use array processors for any of the demonstrations in this paper or in part II (Ref. 11). We were able (due to computational efficiency) to get sufficiently long-time behavior using a VAX-750 computer as is demonstrated in part II (Ref. 11).

It is generally believed that the noise effect is unimportant for the late stages of phase-separation kinetics.<sup>20</sup> As far as we know, the issue has not yet been settled analytically or numerically. We have briefly addressed this problem in a recent paper<sup>21</sup> and will consider it in detail in part II (Ref. 11). Our study clearly supports the irrelevance of noise. Furthermore, since our main aim in

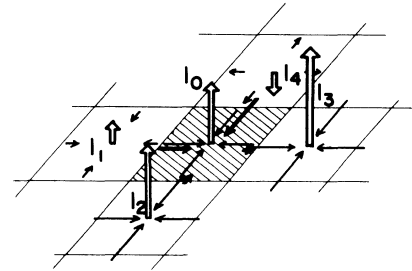


FIG. 2. Intuitive explanation of our model for the conserved case. The white arrows ( $I$ 's) denote  $\mathcal{F} - \psi$  for each cell, the driving force due to the chemical potential. If there is no constraint due to the conservation of the order parameter, each cell has its order parameter updated by an increment proportional to  $I$ . However, when the conservation of the order parameter must be respected, the cell must extract the order parameter from its neighboring cells. The driving force for this extraction is still proportional to  $I$  and is denoted by thin arrows in the plane. However, the same process is occurring in neighboring cells. Thus, on each edge between two cells, two opposing forces meet, and the cell with the longer thin arrow wins. It gains in order parameter by an amount proportional to the difference of  $I$ 's denoted by thick arrows in the figure. Summing over all the cells neighboring a cell, we have that the cell has a net gain proportional to  $I - \langle\langle I \rangle\rangle = \mathcal{F} - \psi - \langle\langle \mathcal{F} - \psi \rangle\rangle$ .

this paper is to propose a new scheme for computationally efficient modeling, we confine ourselves to deterministic models.

C. "Structural stability"

As mentioned in Sec. II B, the choice of  $f$  (which determines the single cell dynamics) is not unique. In most of our simulations, we choose

$$f(x) = A \tanh x, \tag{2.10}$$

where  $A$  is a parameter which is greater than 1. There can be many other choices. To demonstrate the insensitivity of our results to the choice of  $f$ , we compare the following three representative maps:

$$f_1(x) = A \tanh x,$$

$$f_2(x) = \begin{cases} Ax & \text{for } |x| < \frac{1}{A} \\ \text{sgn}(x) & \text{for } |x| \geq \frac{1}{A} \end{cases}, \tag{2.11}$$

$$f_3(x) = \frac{Ax}{[1+x^2(A^2-1)]^{1/2}}.$$

All these maps possess the features we had required in Sec. II B when  $A > 1$ . The motivation for choosing  $f_3$  (see Fig. 19 for its functional form) will become clear in Sec. IV; it arises naturally in the implementation of the new discretization scheme we propose in this paper. We should point out that time scales for these maps depend on the value of the parameter  $A$  which determines the (global) rate of being "pulled" into a fixed point. However, we expect them to give the same asymptotic results. All demonstrations in this paper are results obtained on a two-dimensional  $100 \times 100$  lattice with periodic boundary conditions. To exhibit the evolution of patterns in different cases, we use the same random initial conditions (unless otherwise mentioned) with order parameter values uniformly distributed (using the same random number seeds) between  $\pm 0.125$ . (After one or two iterations, the distribution becomes Gaussian.) All form factors were obtained as averages over 20 independent runs. As explained in detail in part II (Ref. 11), this sample size is insufficient to determine conclusively the scalarized form factor for small values of  $k$ . However, it is large enough to enable us to study the behavior at intermediate and large values of  $k$ .

In Fig. 3, we show evolution patterns due to the iteration of (2.7) (the nonconserved case), using maps  $f_1, f_2,$  and  $f_3$ , with  $A=1.3$  and  $D=0.5$ . The value of  $A$  chosen gives rise to stable fixed points at  $\pm 0.98$  for the map  $f_1$ . Maps  $f_2$  and  $f_3$  have stable fixed points at  $\pm 1$ , independent of the value of  $A$  ( $> 1$ ). The top two pictures of Fig. 3 are for the map  $f_1$ , the middle two are for the map  $f_2$ , and the bottom two are for the map  $f_3$ . They give almost identical patterns at different evolution times. In Fig. 4 we show evolution patterns due to the iteration of (2.9) (the conserved case), using maps  $f_1, f_2,$  and  $f_3$ , with  $A=1.3$  and  $D=0.5$ . Again, the patterns evolve almost identically.

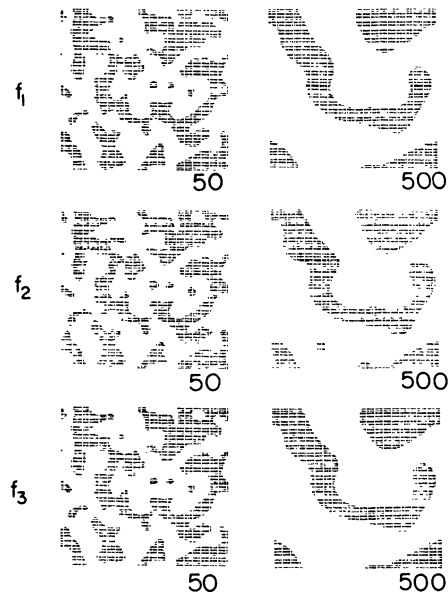


FIG. 3. Evolution patterns for the nonconserved case using maps  $f_1, f_2,$  and  $f_3$  from the same random initial configuration. The top two pictures are for the map  $f_1$ , the middle two are for the map  $f_2$ , and the bottom two are for the map  $f_3$ . The numbers denote necessary time steps from the initial condition. Only points with positive order parameters are marked. This coding is also used in all subsequent evolution patterns we display in this paper.

Perhaps the most interesting feature of the ordering process is the observation of an approximate scaling law in Monte Carlo simulations of the process.<sup>7-9</sup> It should be noted that, previous to these simulation results, Binder and Stauffer<sup>3(a)</sup> and Furukawa<sup>1,3(b)</sup> had already discussed the possibility of scaling behavior. Their arguments and

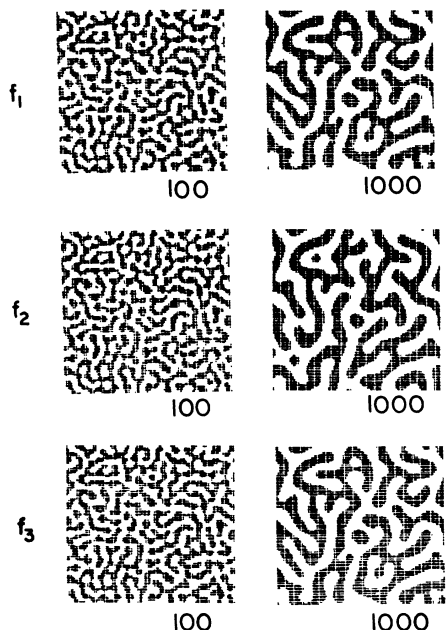


FIG. 4. Evolution patterns for the conserved case using maps  $f_1, f_2,$  and  $f_3$  from the same random initial configuration as in Fig. 3.

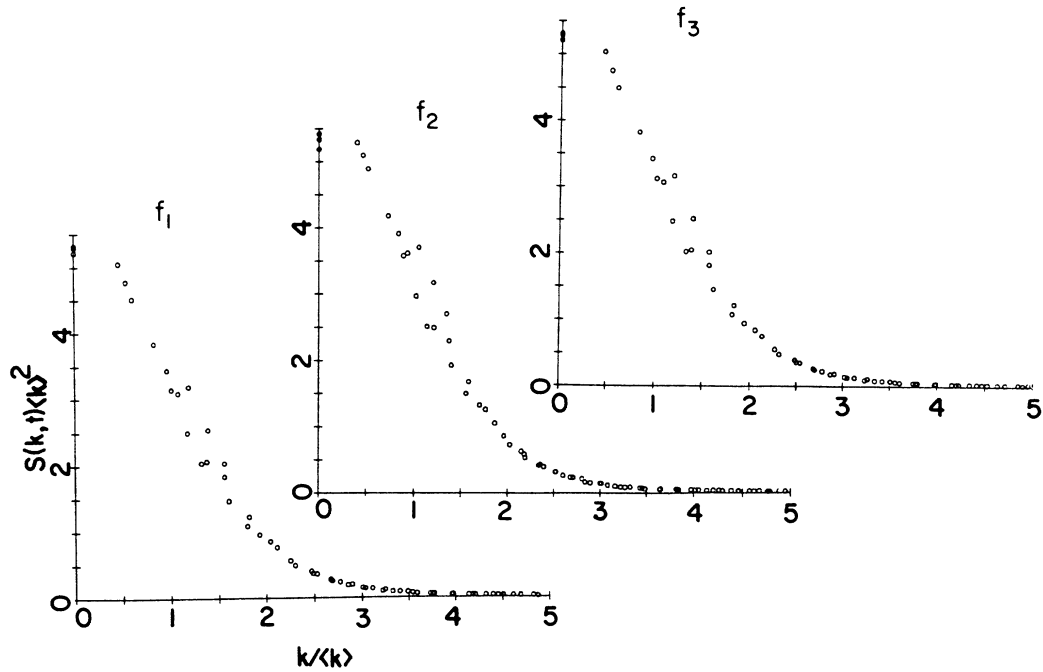


FIG. 5. Scaled form factors for the conserved case for the three different maps. Data from times 50, 100, and 150 are superposed for each plot.

the Monte Carlo results suggested that the normalized (and scalarized) form factor  $S(k, t)$  [which is obtained by circularly averaging the normalized form factor  $S(\mathbf{k}, t)$ ] has a scaling regime in which it behaves as

$$S(k, t) = l(t)^d \Phi(kl(t)), \tag{2.12}$$

where  $k$  is the magnitude of the wave vector  $\mathbf{k}$ ,  $t$  the time,

$\Phi$  a universal function,  $l(t)$  a time-dependent length scale which behaves as  $l(t) \sim t^\phi$  for some positive number  $\phi$ , and  $d$  is the spatial dimensionality. Figures 5 and 6 show the scaled form factors for the nonconserved and conserved cases using the three maps with parameter values as previously. Here we use a somewhat different scaling from that in our previous paper<sup>19</sup> so as to avoid adjust-

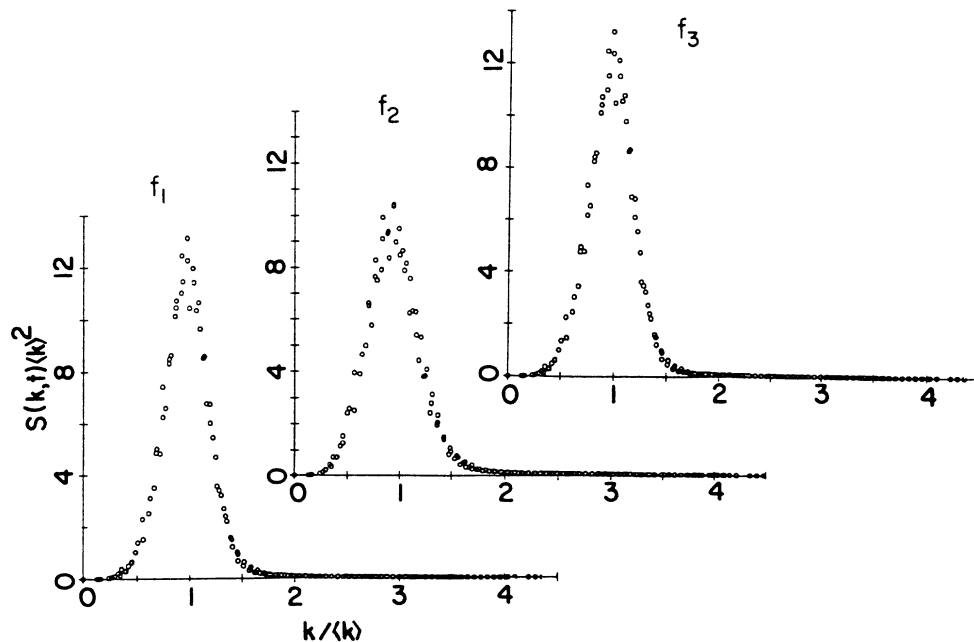


FIG. 6. Scaled form factors for the conserved case for the three different maps. Data from times 600, 900, and 1200 are superposed for each plot.

able parameters. We scale by the quantity  $\langle k \rangle(t)$ ,

$$\langle k \rangle(t) = \int_0^\infty dk k S(k,t) / \int_0^\infty dk S(k,t). \quad (2.13)$$

This is related to the typical domain size as  $\langle k \rangle(t) \propto l(t)^{-1}$ . Thus we would expect that (if the scaling holds good)

$$\langle k \rangle(t) \propto t^{-\phi}. \quad (2.14)$$

Note that  $\langle k \rangle(t)$  is *not* the true average with respect to  $S(\mathbf{k},t)$ ,

$$\bar{k}(t) = \int_0^\infty dk k^d S(\mathbf{k},t) / \int_0^\infty dk k^{d-1} S(\mathbf{k},t). \quad (2.15)$$

As explained in part II (Ref. 11), this quantity is logarithmically divergent in the limit of infinitesimally thin walls. Even though the walls in our simulation are not infinitesimally thin, the quantity  $\bar{k}(t)$  has a strong dependence on the upper cutoff for  $k$ . Hence we prefer to use  $\langle k \rangle(t)$  rather than  $\bar{k}(t)$ .

Numerically, we compute  $\langle k \rangle(t)$  by considering all  $\mathbf{k}$  values up to half the reciprocal lattice size. Notice that  $\mathbf{k}$  can take up values (for a lattice of size  $N \times N$ )  $2\pi(m_x, m_y)/N$ , where  $m_x$  and  $m_y$  have integer values between  $-N/2$  and  $(N/2)-1$ . In Fig. 5 we superpose  $S(k,t)\langle k \rangle(t)^2$  for the nonconserved case as a function of  $k/\langle k \rangle(t)$  for the three different maps for times 50, 100, and 150. The data are seen to lie on a reasonable master curve for the different maps and these master curves are almost identical. In Fig. 6 we present the scaled form factors for the conserved case for times 600, 900, and 1200, again for the three different maps. Here also, we see that the data for each map lie on a reasonable master curve. For maps  $f_1$  and  $f_3$ , these master curves are not the asymptotic curves. Rather, they correspond to the so-called ‘‘soft-wall’’ regime, in which the thickness of the boundary is appreciable relative to the representative pattern size. Long-time simulations are necessary before ‘‘hard-wall’’ behavior is seen and the scaled form factors for the ‘‘hard-wall’’ case appear to approach an asymptotic result.<sup>21</sup> We will elaborate on this in Sec. III C and discuss it in detail in part II (Ref. 11). On the other hand, the scaled form factor for the map  $f_2$  appears to be already close to the asymptotic result. This is because the walls ‘‘harden’’ rapidly for this map. We can easily understand this if we invoke the concept of the free-energy functional (though this is not necessary). The free-energy functional corresponding to map  $f_2$  is shown in Fig. 7. It should be noted that, for deep quenches, this free-energy functional is much more realistic than the  $\phi^4$  functional. Consider a binary alloy without any vacancies. The order parameter is usually defined as the difference  $\phi_A - \phi_B$ , where  $\phi_A$  ( $\phi_B$ ) is the local number density of  $A$  ( $B$ ). Since there are no vacancies,  $\phi_A + \phi_B = \psi_0$  must be constant everywhere and is the total number density of atoms. We have  $\phi_A = (\psi_0 + \psi)/2$  and  $\phi_B = (\psi_0 - \psi)/2$ , both of which must be non-negative. Thus, we should always have  $|\psi| < \psi_0$ . This requires vertical potential walls at  $\psi = \pm\psi_0$ . Between these two walls the free-energy functional should be concave for a deep quench, since the disordered phase is unstable. Thus we have nat-

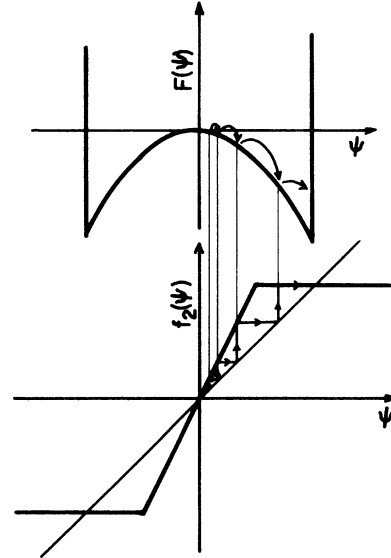


FIG. 7. Free-energy functional corresponding to the piecewise linear map  $f_2$ .

urally arrived at the free-energy functional in Fig. 7. The cusps in the free energy are the result of idealization (or simplification) and do not affect the physics of the process. They can easily be smoothed out without affecting the dynamics of the phase separation. This free-energy functional leads to an interesting partial-differential-equation model, as we discuss in Sec. V.

These results clearly demonstrate that the maps are hard to distinguish. This may be understood as follows. We are interested in the global phase configurations. The majority of cells (except for those near the phase boundaries) have order parameter values close to those of the sinks. The cells near the phase boundary are ‘‘slaved’’ by the cells in the bulk phase. Hence the global behavior is determined by the hyperbolicity of the sinks. This leads us to assert the ‘‘structural stability’’ of our modeling: our CDS models with different maps but with the same flow diagram [Fig. 1(c)] give phenomenologically similar results. Furthermore, the difference of  $f_1$ ,  $f_2$ , and  $f_3$  suggests that the evolution rate is determined by the linearized maps around the sinks. We should add a cautionary remark about our usage of the term ‘‘structural stability.’’ In the standard usage<sup>22</sup> this implies stability under homeomorphisms. Our usage is somewhat different, since we must retain not only the hyperbolicity of the sinks but also their symmetrical positions.

As is implicit in the preceding paragraph, if the map  $f$  is close to the line  $x = y$ , then the bulk phase is not sufficiently stable and the origin is not sufficiently unstable. Then, as long as the typical pattern size is small, the dynamics is strongly affected by the phase boundary. The phase-boundary dynamics reflects the shape of the map, so that the results at this stage need not be universal. However, if we wait long enough, the thickness of the phase boundary becomes small compared to the representative size of the bulk phases. At that stage, we expect the details of the map to be washed away. This corresponds to the transition from soft-wall to the late stage hard-wall behavior.<sup>21</sup>

### III. DEMONSTRATIONS

As has already been mentioned in our Introduction, the main body of the results obtained by our scheme will be given in Ref. 11. Here we discuss representative examples in order to show the potential of our scheme.

#### A. Relation to microscopic “reality”

To compare our results with real experimental results, we must specify two numerical parameters in the CDS model,  $A$  and  $D$ . At present, there is no way to derive the CDS models from a more microscopic description of the systems. Hence these parameters are purely phenomenological. However, the same is true of parameters in partial-differential-equation models like the CH equation. Consequently, there is *no* fundamental difference between CDS and partial-differential-equation models in their relation to reality.

The true predictions of the CDS models are, therefore, the results which are independent of adjustable parameters. The situation is the same as that in the renormalization-group theory; true predictions are those which are free of phenomenological length scales. Hence, if there are universal features in the phase-ordering dynamics, they should be captured by phenomenological models like ours. Of course, the universal features (if any) are described by a particular model only if the physical system is in the same universality class as the model used. Whether our CDS models (and the conventional partial-differential-equation models) are in the same universality class as systems we wish to describe can be ascertained, strictly speaking, only through a comparison of our results with those from experiments.

From the preceding paragraph, one might argue that results which depend on the choice of parameters  $A$  and  $D$  are meaningless; since our model is not a faithful description of “microscopic reality,” the nonuniversal behaviors should not be discussed with the aid of this type of model. We should notice, however, that nonuniversal features need not depend on the extreme details of the system. Rather, there should be “weak” universal features which can be captured by adjusting phenomenological parameters. A good example is the Debye theory for specific heat. The universal feature is the so-called  $T^3$  asymptotic law. The deviation from this universal law can be successfully captured by a single parameter, the Debye temperature. As we will see, the soft-wall effect in spinodal decomposition is a good example of this “weak universality.”

Since we have demonstrated the “structural stability” of our CDS model, we choose the  $\tanh(f_1)$  model for all further demonstrations in this paper. One may wonder why we do not use the map  $f_2$ , which appears to reach the asymptotic form factor in a shorter iteration time. Our motivation for the choice of  $f_1$  is the smoothness of the map and the analytic advantages this would offer. Besides, the  $\tanh$  map is remarkably close to the map dictated by the new discretization scheme we propose in Sec. IV. We can also choose different parameter values which give an equally rapid evolution for the  $\tanh$  map. Equally well, by choosing  $A$  sufficiently close to 1 for the map  $f_2$ , we can simulate the soft-wall to hard-wall evolution.

Parameters  $A$  and  $D$  fix the wall (kink) thickness and the time scale. As discussed above, if we want to describe a real experiment,  $A$  and  $D$  become adjustable parameters; there is no reliable way to calculate them from microscopic models. Here we exhibit configurations and form factors for the nonconserved- and conserved-order-parameter cases, in turn. Note that if we choose  $A$  too large or  $D$  too small, the patterns may be frozen. This corresponds to trapping in metastable states in Monte Carlo simulations. The range of  $(A, D)$  values in which freezing does not occur will be discussed in Sec. IV C.

#### B. Nonconserved-order-parameter case

For the sake of convenience, we reproduce here our CDS model (2.7) for the nonconserved case:

$$\begin{aligned} \psi(t+1, n) &= f(\psi(t, n)) + D[\langle\langle \psi(t, n) \rangle\rangle - \psi(t, n)] \\ &\equiv \mathcal{F}[\psi(t, n)], \end{aligned} \quad (3.1)$$

where we use  $f(x) = A \tanh x$ . As mentioned earlier, all of our demonstrations (for both the nonconserved and conserved cases) here are for a two-dimensional  $100 \times 100$  lattice with periodic boundary conditions. The parameter values used (unless otherwise mentioned) are  $A=1.3$  and  $D=0.5$ . These parameter values correspond to a deep quench. All calculations were done on a VAX-750 computer (without using any array processors). For the nonconserved case, a single update of the lattice took 1.54 CPU seconds. (In Ref. 18, the update time reported was 1.98 CPU seconds. The reduction in time is the result of a number of changes we have incorporated into our programs. These do *not* include using a lookup table for the dynamics. In the conserved case, the reduction is even more appreciable. The update time for a  $100 \times 100$  lattice is now 1.77 CPU seconds, as opposed to the earlier reported value of 3.33 CPU seconds.<sup>19)</sup>

Figure 8 shows a typical evolution pattern using (3.1), resulting from the random initial configuration we use for most of the evolution patterns, i.e., with order parameter values uniformly and randomly distributed between  $\pm 0.125$  (labeled by 0 in the figure). As can be seen from Fig. 8, well-developed patterns appear within 20 updates. In Fig. 9(a), we have plotted  $S(k, t) \langle k \rangle(t)^2$  as a function of  $k / \langle k \rangle(t)$  for times 100, 200, 300, 400, and 500. The solid line is the analytic form provided by Ohta *et al.*<sup>20</sup> The agreement is not good at small values of  $k / \langle k \rangle(t)$  due to the poor statistics at small  $k$  and the finite-size effects [see part II (Ref. 11)]. However, the data for longer times lie closer to the theoretical predictions, suggesting that the system has yet to reach the scaling regime if any. This is borne out by Fig. 9(b), in which we have plotted  $\ln[S(k, t) \langle k \rangle(t)^2]$  as a function of  $k / \langle k \rangle(t)$  for the same times as above. The tail of our curve is not yet compatible with Porod’s law,<sup>23</sup> which predicts that the tail decays as  $x^{-3}$  in two space, where  $x = k / \langle k \rangle$ . The decay of the tail is stronger than  $x^{-3}$  as the result of the nonzero thickness of the wall [see part II (Ref. 11)]. Monte Carlo results, on the other hand, give a tail that falls off as  $x^{-2.5}$  (Ref. 7) due to the raggedness of the interface. The tail of the numerically obtained curve moves up in time and approaches the theoretical prediction. Unfortunately, for a  $100 \times 100$  system, we are un-

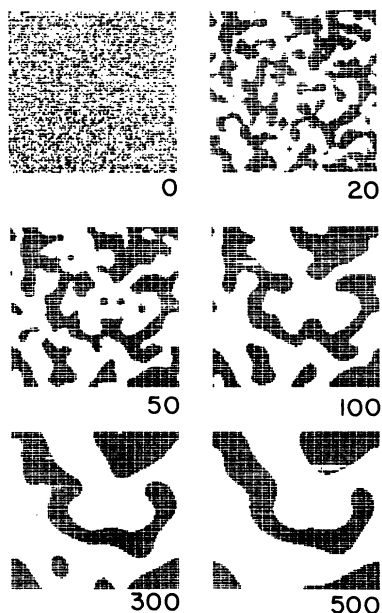


FIG. 8. Long-time evolution patterns for the nonconserved case using the tanh map ( $f_1$ ). The random initial configuration is the same as that used previously and is labeled by 0 in the figure.

able to go further in time because the pattern size is a sizable fraction of the lattice size by 500 steps. In part II (Ref. 11), we will present results from a larger lattice size. We should point out a mistake in our previous letter.<sup>19</sup> There, we had used an adjustable parameter to compare our numerical results with the theoretical prediction. Scaling by this parameter, we had matched the  $k=0$  values of our numerical results with the theoretical curve and concluded that the only discrepancy was in the tail. Our present results (without any adjustable parameter) prove that conclusion to be incorrect. The true conclusion should be that, in both small and large  $k/\langle k \rangle$  regions, our results up to 500 steps do not agree with the formula derived by Ohta *et al.*;<sup>20</sup> however, there is a strong indication that the discrepancies diminish considerably at later times.

### C. Conserved-order-parameter case

For the sake of convenience, we reproduce our CDS model (2.9) for the conserved case:

$$\psi(t+1, n) = \mathcal{F}[\psi(t, n)] - \langle \mathcal{F}[\psi(t, n)] - \psi(t, n) \rangle. \quad (3.2)$$

As already mentioned, a single update of (3.2) for a  $100 \times 100$  lattice with periodic boundary conditions took 1.77 CPU seconds.

*Critical quench.* The case of critical quenching is the most interesting one and is analytically the least tractable. It corresponds to the situation when the spatial integral of the order parameter is zero,

$$\int d\mathbf{r} \psi(\mathbf{r}, t) = 0.$$

In Fig. 10 we show a typical evolution pattern resulting

from (3.2) for long times. In Fig. 11 we have plotted  $S(k, t) \langle k \rangle(t)^2$  as a function of  $k/\langle k \rangle(t)$  for times 1800, 2400, 3000, 3600, and 4200. These corresponds to times on both sides of an exponent crossover from  $\sim 0.28$  to  $\sim 0.33$ .<sup>21</sup> [Huse<sup>9(b)</sup> has claimed (by extrapolation) an asymptotic exponent of  $\sim 0.33$  in his Monte Carlo simulations of the conserved case.] The shape of the function seems insensitive to the value of the exponent at that time. Unfortunately, in this case, there is no theoretical prediction for us to make a comparison with. Again, our numerical curve does not satisfy Porod's law<sup>23</sup> and falls off faster than  $x^{-3}$ , where  $x = k/\langle k \rangle(t)$ .

*Critical quench, soft-wall case.* As mentioned earlier, our parameter values correspond to a deep quench. This quickly results in sharp domain walls, whose thickness is negligible in comparison to the representative pattern size. This is the so-called hard-wall case. We can also simulate the so-called soft-wall case by considering a quench which is not so deep, i.e., by choosing  $A$  close to 1. In this case, the domain wall thickness stays appreciable compared to the representative pattern size for a considerably longer time. Recall that the representative pattern size behaves as  $t^\phi$ . The exponent  $\phi$  changes in time from  $\sim 0.27$  to  $\sim 0.33$ .<sup>21</sup> The soft-wall evolution results in a delay of the crossover in the exponent.<sup>21</sup> We will discuss this in detail in part II (Ref. 11). Here we show a representative evolution pattern (Fig. 12) for the soft-wall case, obtained by using  $A=1.2$  and  $D=0.5$  in (3.2). In Fig. 13, we show the scaled form factors for the soft-wall case for times 2000, 2800, 3600, 4400, and 5200. They are similar to the early time form factors shown in Fig. 6 for maps  $f_1$  and  $f_3$  with  $A=1.3$ .

*Anisotropy effect.* As mentioned in Sec. II, an anisotropy effect is introduced if we do not choose a proper discretization of the Laplacian. For example, the usual form of the discretized Laplacian for the square lattice corresponds to the following choice of  $\langle \langle \psi(t, n) \rangle \rangle$ :

$$\langle \langle \psi(t, n) \rangle \rangle = \frac{1}{4} \sum (\psi \text{ in the nearest-neighbor cells}). \quad (3.3)$$

Using this form makes no difference in the nonconserved case. However, in the conserved case, especially with large  $A$ , this gives rise to patterns which are preferentially inclined along the [10] and [01] directions, especially at later stages of the evolution. A representative evolution pattern is shown in Fig. 14 from the same initial condition as previously, though with parameters  $A=1.3$  and  $D=0.4$ . The parameter values we have been using earlier ( $A=1.3$  and  $D=0.5$ ) give rise to an arithmetic overflow in this case. We are presently investigating the stability of (3.2) with the anisotropic Laplacian. The corresponding form factors (which we do not show here) do not show good scaling. We have also tried a form of  $\langle \langle \psi(t, n) \rangle \rangle$  with nearest and next-nearest neighbors having equal weight. This gives rise to patterns which are preferentially inclined along the [11] and  $[1\bar{1}]$  directions.

*Spinodal decomposition with off-critical quench.* It is also possible to quench the system off-critically with

$$\int d\mathbf{r} \psi(\mathbf{r}, t) \neq 0.$$

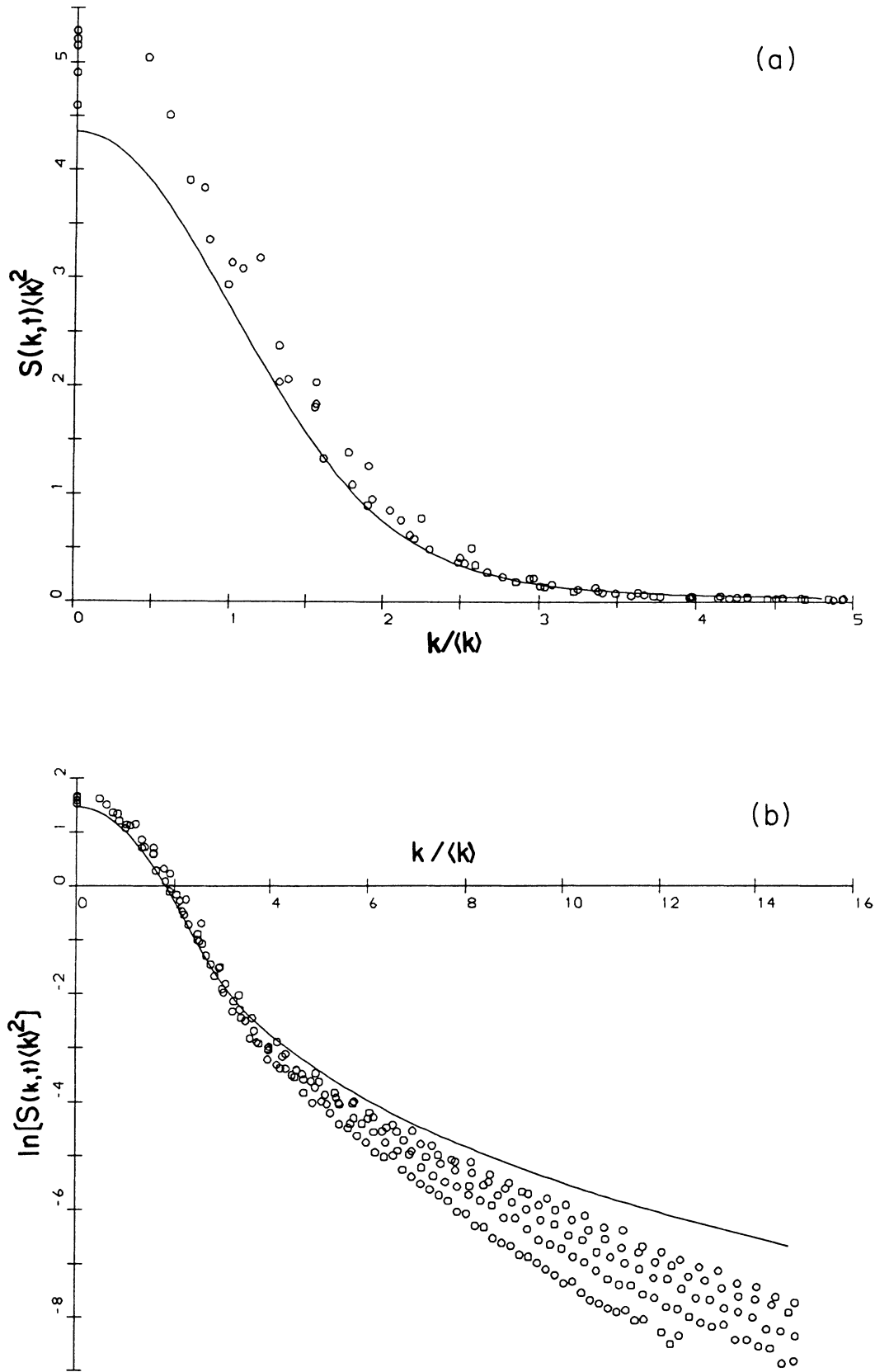


FIG. 9. (a) Scaled form factors for the nonconserved case for the tanh map. Data from times 100, 200, 300, 400, and 500 are superposed. The solid line is the analytic form provided by Ohta *et al.* (Ref. 20). There are no adjustable parameters in these scaled form factors. The best agreement between our results and the theory is for the data at time 500. (b) Semilogarithmic plot of scaled form factors from (a) which shows the structure of the tail. It shifts upward in time, towards the analytic form of Ohta *et al.* (Ref. 20).

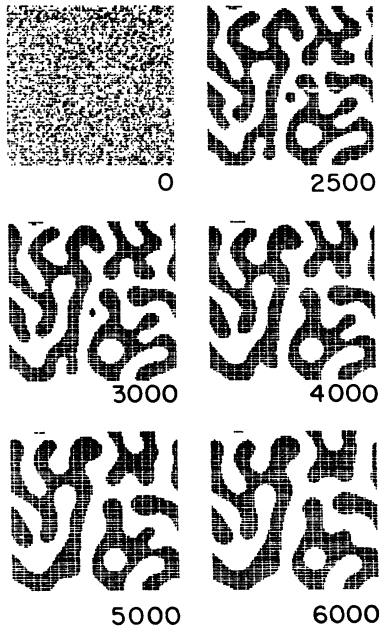


FIG. 10. Long-time evolution patterns for the conserved case using the tanh map. The random initial configuration is the same as that used previously.

Depending on whether the system is in an unstable state or a metastable state after quenching, the phase ordering proceeds via either spinodal decomposition or the so-called “nucleation process.” Here, we exhibit the case of off-critical quench with the system segregating via spinodal decomposition.

We simulate an off-critical quench by appropriately biasing the random initial configuration. In Fig. 15, we show a typical evolution pattern from an initially random configuration with the order parameter uniformly distributed between  $-0.3 \pm 0.125$ . Clustering, necking, and evaporation of clusters are evident in the evolution process. In Fig. 16, we show the scaled form factors for the off-critical quench for times 600, 900, and 1200. Again, there is no theoretical prediction for us to make a comparison with.

*Nucleation regime.* In a highly off-critical quench, the uniform state of the system is a metastable state. Segregation of phases can occur only if nucleation centers exist. In our deterministic model, we have to put in nucleation centers (“seeds”) by hand.

We simulate the nucleation regime by considering a random initial configuration uniformly distributed between  $-0.6 \pm 0.125$  with randomly placed seeds (each consisting of at least four sites each and adding up to

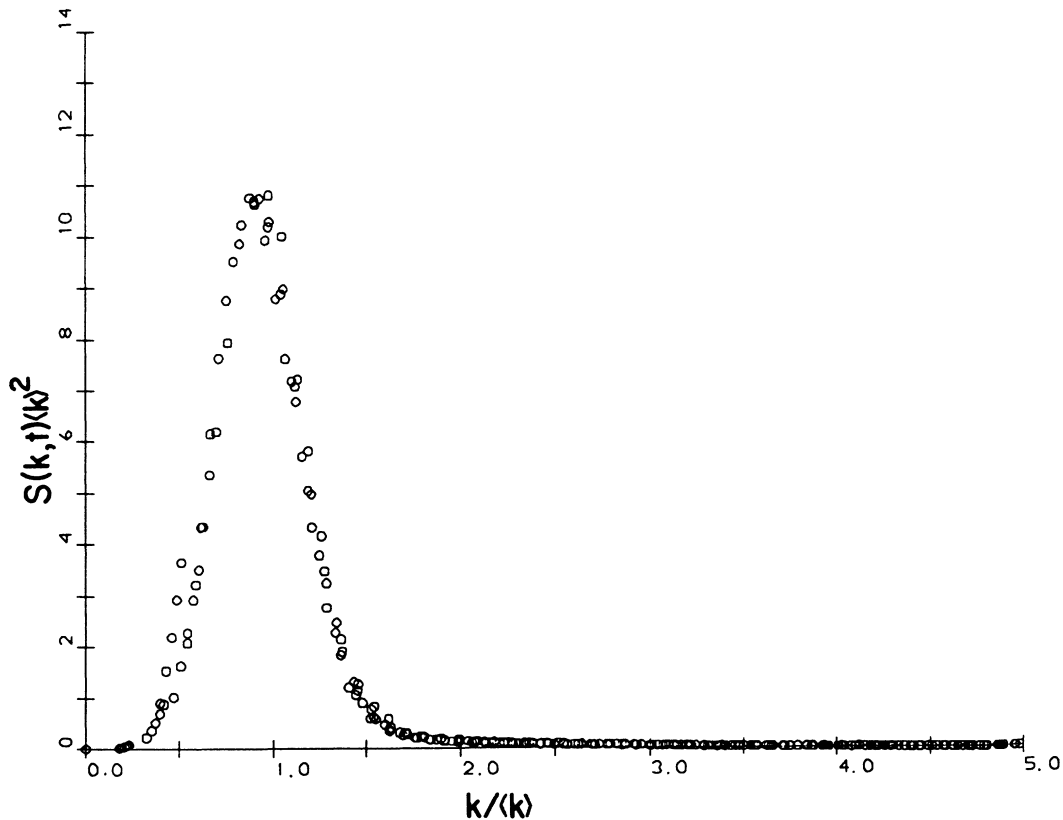


FIG. 11. Scaled form factors for the conserved case for the tanh map. Data from times 1800, 2400, 3000, 3600, and 4200 are superposed. These times correspond to both sides of an exponent crossover from  $\frac{1}{4}$  to  $\frac{1}{3}$  (Ref. 21).

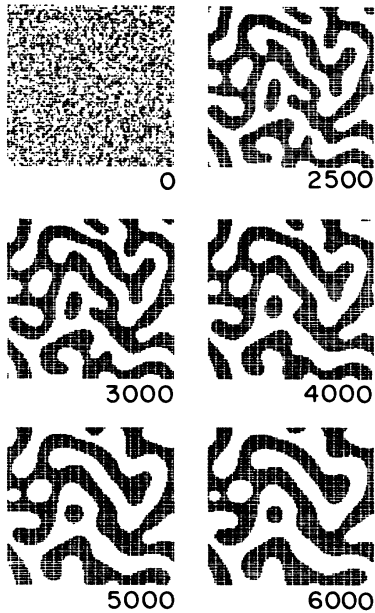


FIG. 12. Long-time evolution patterns for the conserved case with a soft-wall evolution. Again, we use the same initial condition as previously.

about 10% of the lattice) of order parameter value  $+0.98$ . We then bias the sites with negative order parameters so that the average order parameter at each site is  $-0.6$ , corresponding to a minority species concentration of 20%. Figure 17 shows the evolution pattern from such an initial condition. In Fig. 18, we show the scaled form factor for this process for times 600, 900, and 1200. In the limit of vanishingly small proportion of one phase, the form factor for this process has been analytically calculated by Ohta.<sup>4(c)</sup> This problem has also recently been studied by Kawasaki *et al.*<sup>(4b)</sup> Unfortunately, we are unable to compare our numerical results with these works because their validity is limited to when the minority species concentration is less than about 10%.

#### IV. RELATION BETWEEN CDS AND PARTIAL DIFFERENTIAL EQUATIONS

As we have shown in the derivation of CDS models in Sec. II, we do not need any partial-differential-equation description of the system to construct a CDS model. Nevertheless, it is a historical fact that partial differential equations have been used almost exclusively to model various physical phenomena. Thus, it would be useful to

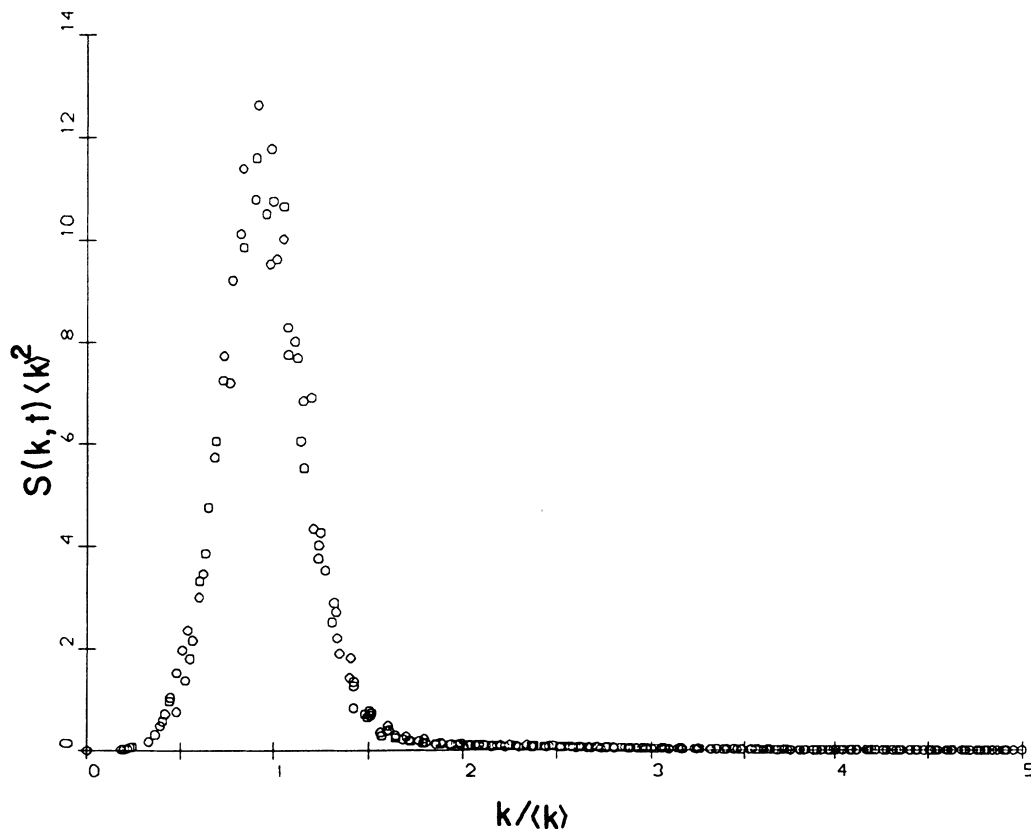


FIG. 13. Scaled form factors for the conserved case with soft-wall evolution. Data from times 2000, 2800, 3600, 4400, and 5200 are superposed. The master curve is similar to those in Fig. 6 for  $f_1$  and  $f_3$ , which represent the early time behavior of the deep quench case.

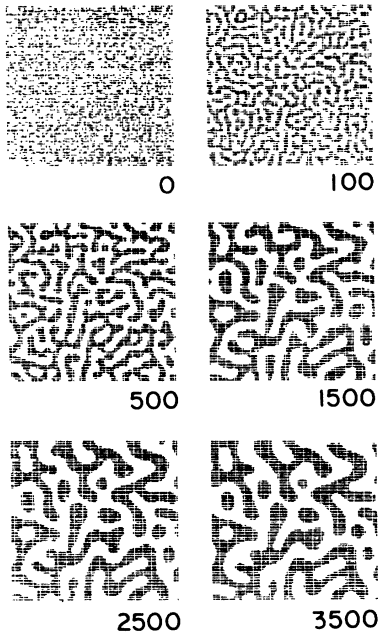


FIG. 14. Long-time evolution patterns for the conserved case with naively discretized Laplacian, i.e.,  $\langle\langle\psi(t,n)\rangle\rangle$  defined by (3.3). The initial condition is the same as before. The pattern at time 3500 should be compared with the pattern at time 2500 in Fig. 12, as the smaller value of  $D$  gives a considerably slower evolution in this case. Comparing these patterns, we see that the pattern at time 3500 has a tendency to be preferentially inclined along the  $[10]$  and  $[01]$  directions.

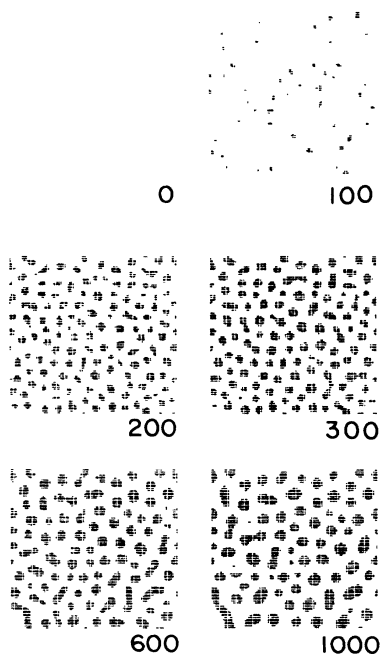


FIG. 15. Evolution patterns for the conserved case with an off-critical quench. The random initial configuration has the order parameter uniformly distributed between  $-0.3 \pm 0.125$ . Clustering, necking, and cluster evaporation are evident in the later stages.

have a relation between partial-differential-equation models and CDS models.

In a trivial sense, the conventional discretization of a partial differential equation yields a CDS. However, our CDS models are not the outcome of a simple discretization of the partial differential equations describing the same phenomena. For example, if we discretize the deterministic (without noise) TDGL equation by the simple Euler scheme, we get

$$\psi(t + \Delta t, n) = \psi(t, n) + \Delta f(\psi(t, n)) + \frac{2d\Delta t}{(\Delta x)^2} L[\langle\langle\phi(t, n)\rangle\rangle - \psi(t, n)], \quad (4.1)$$

where  $\Delta x$  and  $\Delta t$  are, respectively, the space and time increments;  $n$  is a vector that labels the site whose position vector is  $x$  ( $n\Delta x = x$ ); and  $d$  is the spatial dimensionality. For the case where  $H[\psi(\mathbf{r}, t)]$  is the  $\phi^4$  free-energy functional given by (2.2), we have

$$f(\psi(t, n)) = L[\tau\psi(t, n) - g\psi(t, n)^3].$$

If we choose a large time increment, then the nonlinear term produces a map which exhibits chaos. Thus the system is a coupled chaotic map system, which is qualitatively different from the original equation or from the system we wish to model. Many pathologies in numerical schemes can be traced to chaos.<sup>24</sup> In our CDS modeling, however, the map is designed to be injective so that there cannot be any chaos.

In this section, we propose a new discretization scheme for semilinear parabolic equations. The scheme gives our CDS model from the deterministic TDGL equation. Then we discuss the convergence and stability of the scheme. The main purpose of this section is to advocate the concept of *qualitative numerical analysis*, which we try to motivate (loosely) later.

#### A. A new discretization scheme

Consider a general semilinear parabolic equation

$$\frac{\partial\psi}{\partial t} = f(\psi) + L\nabla^2\psi, \quad (4.2)$$

where the symbols have their usual meaning. The instability of numerical schemes is often due to the nonlinearity of the function  $f$ , as we mentioned earlier. Hence, if we can eliminate instabilities due to this nonlinearity, we may have a more efficient scheme by being able to choose a larger time increment than in the conventional schemes. When  $f$  is the logistic function [ $f(\psi) = \lambda\psi(1 - \psi)$ , where  $\lambda$  is a positive parameter], there are several ingenious schemes for stabilizing the iteration, e.g., implicit schemes.<sup>25</sup> However, it may not be easy to find such a scheme for an arbitrary  $f$ . We propose here an algorithm which produces a stable discretization scheme for an arbitrary  $f$ .

Our proposal is to use the solution semigroup for the spatially uniform problem to discretize semilinear parabolic equations. Let  $F_s$  be the solution semigroup for the ordinary differential equation corresponding to (4.2),

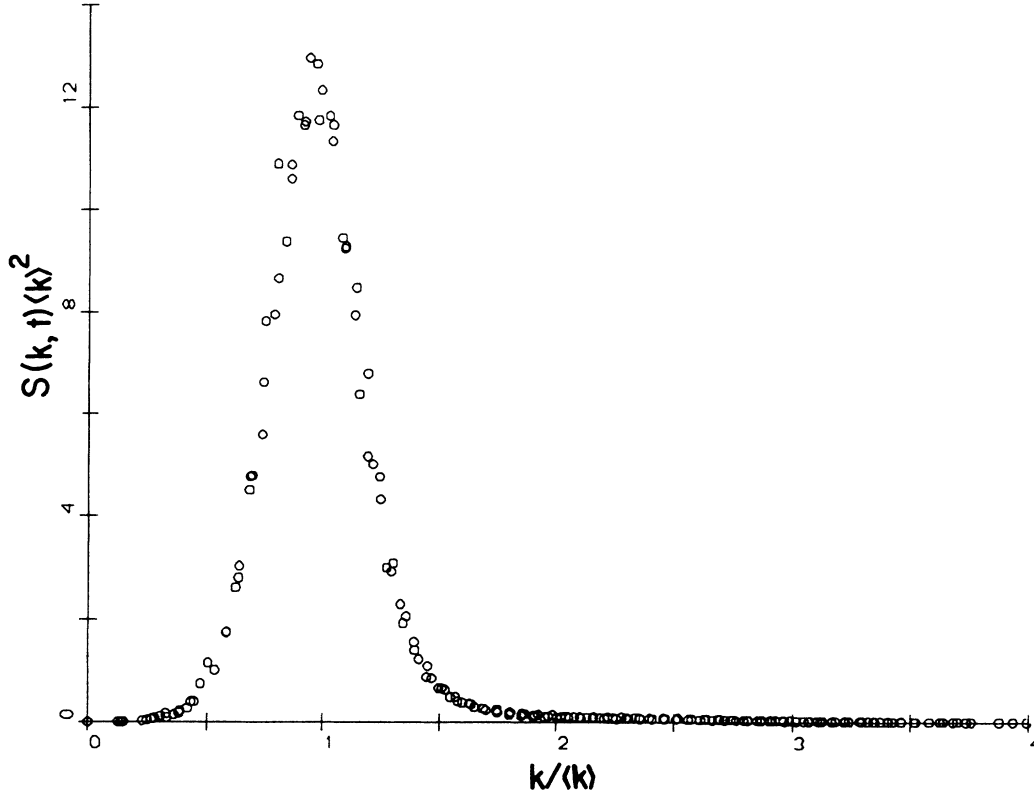


FIG. 16. Scaled form factors for the conserved case with an off-critical quench. Data from times 600, 900, and 1200 are superposed.

$$\frac{d\psi}{dt} = f(\psi), \quad (4.3)$$

such that

$$\psi(t+s) = F_s(\psi(t)). \quad (4.4)$$

This  $F_s$  may not always be obtainable analytically, but this does not present a major obstacle. After all, it is common to use a lookup table for a function so as to accelerate the computation. For the present purpose, its existence is enough. Using the semigroup map, we discretize the original partial differential equation. The most naive scheme may be

$$\begin{aligned} \psi(t+\Delta t, n) \\ = F_{\Delta t}(\psi(t, n)) + 2\gamma[\langle\langle \psi(t, n) \rangle\rangle - \psi(t, n)], \end{aligned} \quad (4.5)$$

where we have put  $\gamma = [d\Delta t / (\Delta x)^2]L$ .

To illustrate the preceding paragraph, let us consider a typical example of the well-known logistic reaction diffusion equation (Fisher equation) with the corresponding ordinary differential equation

$$\frac{d\psi}{dt} = \lambda\psi(1-\psi), \quad (4.6)$$

where  $\lambda$  is a positive parameter. The Euler discretization scheme gives

$$\psi(t+\Delta t) = \psi(t) + \lambda\Delta t\psi(t)[1-\psi(t)], \quad (4.7)$$

where  $\Delta t$  is the time increment. With a large time incre-

ment, the discretized version exhibits chaos. Of course, no chaos is possible in the original ordinary differential equation. In the present example we can explicitly solve the Cauchy problem to get the solution semigroup  $F_s$  as

$$\begin{aligned} \psi(t+s) &\equiv F_s(\psi(t)) \\ &= \frac{\psi(t)}{\psi(t) + [1-\psi(t)]e^{-\lambda s}}. \end{aligned} \quad (4.8)$$

This is a discretized mapping as before, but in this case the map is trivially injective due to the uniqueness of the solution to the Cauchy problem.

The CDS model we have been using for the nonconserved-order-parameter case is essentially the same as (4.5). For the ordinary differential equation corresponding to the deterministic TDGL equation (with the  $\phi^4$  free-energy functional), the solution semigroup reads

$$\begin{aligned} \psi(t+s) &= F_s(\psi(t)) \\ &= \frac{a\psi(t)}{[a^2e^{-2L\tau s} + \psi(t)^2(1-e^{-2L\tau s})]^{1/2}}, \end{aligned} \quad (4.9)$$

where  $a = \sqrt{\tau/g}$ . Replacing this in (4.5) and rescaling as

$$\begin{aligned} 2L\tau t &\rightarrow t', \\ 2L\tau(\Delta t) &\rightarrow (\Delta t'), \end{aligned} \quad (4.10)$$

$$\frac{\psi}{a} \rightarrow \psi',$$

we have (dropping the primes)

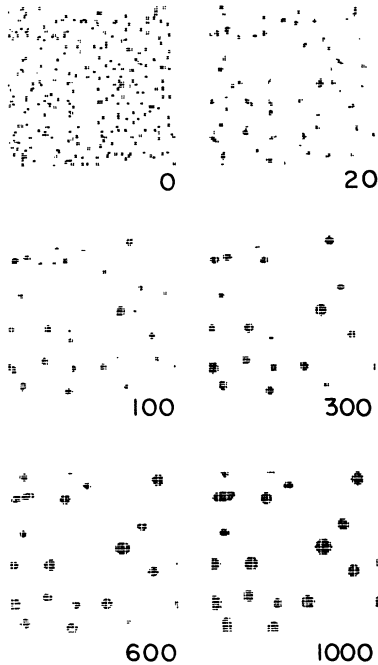


FIG. 17. Evolution patterns for the conserved case in the nucleation regime. The random initial configuration is constructed by having the order parameter uniformly distributed between  $-0.6 \pm 0.125$  with randomly placed seeds (each consisting of at least four sites each and adding up to about 10% of the lattice) of order parameter  $+0.98$ . The sites with negative order parameter are then biased so that the average order parameter at each site is  $-0.6$ , corresponding to a minority species concentration of 20%.

$$\psi(t + \Delta t, n) = \frac{\psi(t)}{[e^{-\Delta t} + \psi(t)^2(1 - e^{-\Delta t})]^{1/2}} + \frac{\gamma}{L\tau} [\langle \psi(t, n) \rangle - \psi(t, n)]. \quad (4.11)$$

Putting  $e^{-\Delta t} = 1/A^2$  and  $\gamma/L\tau = D$  we have

$$\psi(t + \Delta t, n) = \frac{A\psi(t)}{[1 + \psi(t)^2(A^2 - 1)]^{1/2}} + D[\langle \psi(t, n) \rangle - \psi(t, n)]. \quad (4.12)$$

This explains our choice of the map  $f_3$  in Sec. II C. We plot this function in Fig. 19 and notice that it looks similar to the tanh map. Since we know (at least empirically) that the system is “structurally stable,” minor differences are unimportant.

If we use the conventional Euler scheme to discretize (2.1) with the  $\phi^4$  free-energy functional, we have

$$\psi(t + \Delta t, n) = (1 + L\tau\Delta t)\psi(t, n) - gL\Delta t\psi(t, n)^3 + 2\gamma[\langle \psi(t, n) \rangle - \psi(t, n)]. \quad (4.13)$$

Using the same rescaling as previously, we have

$$\psi(t + \Delta t, n) = \bar{A}\psi(t, n) - (\bar{A} - 1)\psi(t, n)^3 + D[\langle \psi(t, n) \rangle - \psi(t, n)], \quad (4.14)$$

where we have put  $\bar{A} = 1 + \Delta t/2$ . For small  $\psi$ , we can match the schemes (4.12) and (4.14) by putting  $A = \bar{A}$ . For the parameter value  $A = 1.3$ , this would correspond to  $\Delta t = 0.6$  in (4.14), which is outrageously high for the

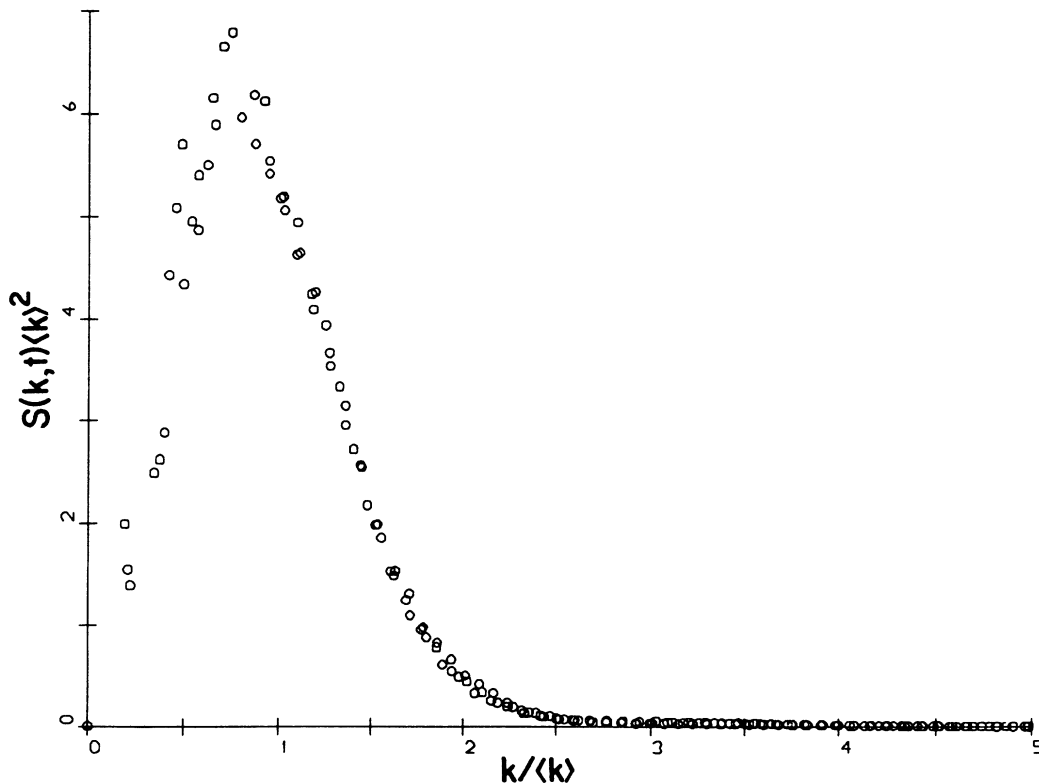


FIG. 18. Scaled form factors for the conserved case in the nucleation regime. Data from times 600, 900, and 1200 are superposed.

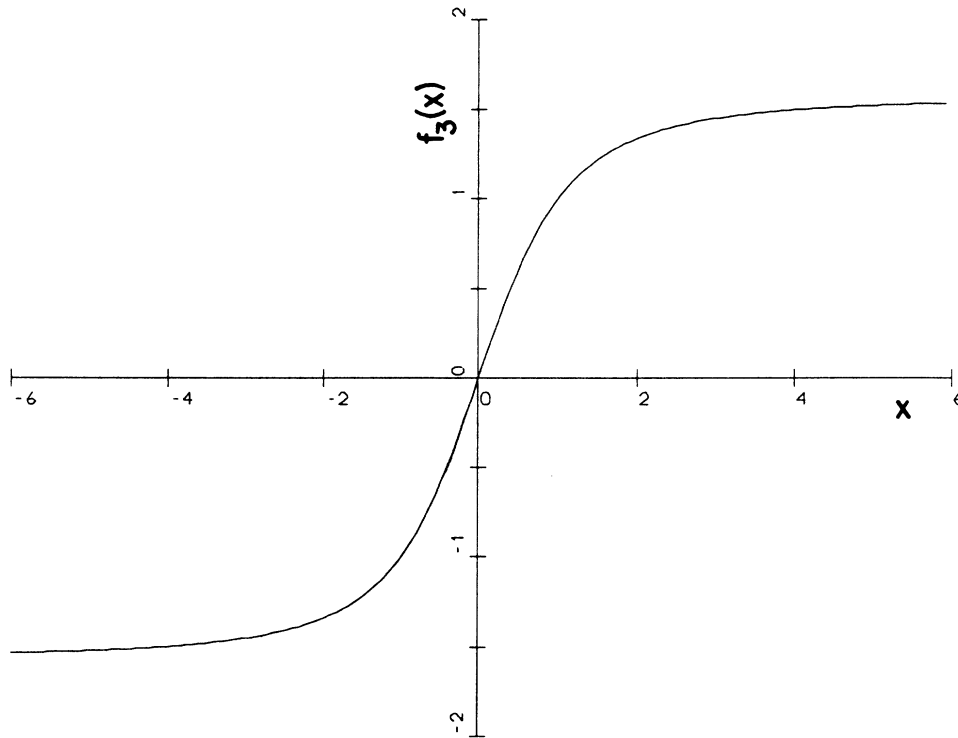


FIG. 19. Functional form of the map  $f_3$  with the parameter value  $A=1.3$ .

Euler scheme. Alternatively, we could match the slopes of the maps at the fixed points, as these appear to determine the rate of pattern evolution. For the parameter value  $A=1.3$  this would require  $\bar{A}=1.204$  and  $\Delta t=0.408$  in (4.14). This is still too high for the Euler scheme. Thus, even though it is possible to get reasonable results by using an appropriate cubic map in the CDS modeling,<sup>12(c)</sup> the time steps involved are so large that the justification of the model should not be in terms of a Euler discretization of the deterministic TDGL equation.

To discretize the CH equation, the best scheme is to discretize the term inside the outermost Laplacian according to the above scheme and then discretize the Laplacian, interpreting it as a mere local averaging operator. Then we arrive at the CDS model used above for the conserved-order-parameter case.

There are many other schemes conceivable even with the use of the solution semigroup. This will be discussed in Sec. IV C. A trivial but interesting feature common to all these schemes is that they give (by design) exact results if the solution is spatially uniform. None of the discretization schemes we are aware of have this property. We may expect that our scheme has advantages over conventional schemes when the spatial dependence is weak.

#### B. Convergence of the proposed scheme

We consider the case of small time increment, which is the major concern in conventional numerical analysis.

We construct a continuous function  $\psi(t,x)$  by linearly interpolating the solution  $\{\psi(m\Delta t,n)\}$  where  $m,n$  are integers, to (4.5).

*Proposition 1.* Let  $T$  be an arbitrary positive number. The linear interpolation of  $\{u(m\Delta t,n)\}$  converges to the correct solution of the original partial differential equation for  $0 < t < T$  in the limit  $\Delta t \rightarrow 0$ , if  $\gamma < \frac{1}{2}$ .

The proof of this proposition is routine with the aid of the mean-value theorem and the Ascoli-Arzelà theorem. It tells us that the scheme is at least as reasonable as the conventional ones. Notice that the proposition is not necessarily trivial, as there are examples of difference schemes which give “approximate” solutions which *do not* converge [(as space and time increments go to zero) to the correct solutions to the original differential equations,<sup>26(a)</sup> e.g., some of the discretization schemes used in lattice-gauge-theory simulations (e.g., species doubling<sup>26(b)</sup>)].

#### C. Qualitative numerical analysis

As was demonstrated in Sec. II, the exact form of the map  $F$  was not crucial, only some basic features of the map need be respected. This implies that, in the proposed scheme, the time increment need not be small to extract universal results. Clearly, if we desire to keep small, say, the  $L^2$  distance between the approximant and the true solution of the differential equation for large  $T$ , then we must keep the time increment sufficiently small. However, we are not interested in the exact numerical re-

sults for the original partial differential equations. There is nothing sacred about the TDGL or CH equations. Our main interest lies in the reality (supposedly) captured by these model equations and not in the equations themselves. Hence accurate numerical simulations of these model differential equations are not crucial in understanding the reality. After all, nature does not give us these equations, but rather the phenomena they attempt to model.

Thus, for these partial differential equations, what we need are numerical schemes which preserve important qualitative features of the true solutions to the partial differential equation; this suggests the concept of *qualitative numerical analysis*. In this section we show the stability of schemes originated from the considerations of Sec. IV B when certain (usually satisfied) conditions hold. This property is a prerequisite for qualitative numerical analysis. Unfortunately, the qualitative theory of partial differential equations is much less developed than that for ordinary differential equations. However, there are a few mathematical results which clearly point in this direction. We will mention some of these later.

For small  $\Delta t$ ,  $F_{\Delta t}(\psi) - \psi$  is of order  $\Delta t$ , so that the following discretization scheme is also adequate as an alternative to (4.5):

$$\begin{aligned} \psi(t + \Delta t, n) &= F_{\Delta t}(\psi(t, n)) + 2\gamma[\langle\langle F_{\Delta t}(\psi(t, n)) \rangle\rangle \\ &\quad - F_{\Delta t}(\psi(t, n))] \\ &= (1 - 2\gamma)F_{\Delta t}(\psi(t, n)) \\ &\quad + 2\gamma\langle\langle F_{\Delta t}(\psi(t, n)) \rangle\rangle, \end{aligned} \tag{4.15}$$

where we have put  $\gamma = [d\Delta t / (\Delta x)^2]L$ . This scheme is intuitively understandable; if the diffusion is slower than the cell relaxation, we should use this scheme. When the cell size is semimacroscopic, this should be true, as diffusion only takes place on the surface of the cell. Notice that, unless the  $\psi$  field takes extremely big values, the schemes (4.5) and (4.15) are numerically close.

The analog of scheme (4.15) for the deterministic TDGL equation would be (after appropriate rescaling)

$$\begin{aligned} \psi(t + 1, n) &= (1 - D)A \tanh[\psi(t, n)] \\ &\quad + D\langle\langle A \tanh[\psi(t, n)] \rangle\rangle, \end{aligned} \tag{4.16}$$

where we have invoked “structural stability” to use the tanh map. In Fig. 20, we show the evolution pattern for the scheme (4.16) with the same parameter values as previously, i.e.,  $A = 1.3$  and  $D = 0.5$ . The evolution gives rise to similar patterns, as in the previous case. The interesting fact is that the parameter domain in which we can have qualitatively satisfactory results is considerably expanded over that for the scheme (4.5), especially for the important region of  $D < 1$ . In Fig. 21, we compare the “safe” regions of simulation in the  $(A, D)$  plane for schemes (3.1) and (4.16). These regions were obtained by simulations (using a number of different random initial conditions) on a  $40 \times 40$  lattice; we expect the “safe” re-

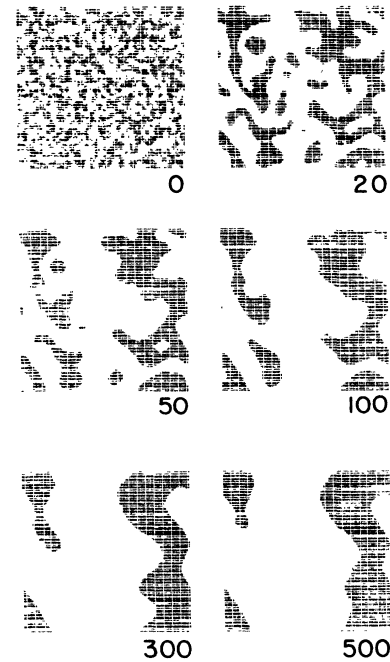


FIG. 20. Evolution patterns for the nonconserved case using the scheme (4.16) with the same initial condition as in Fig. 3, etc.

gion to be larger for a  $100 \times 100$  lattice, as it is harder for the pattern to freeze on a bigger lattice. In Fig. 21, the upper frame corresponds to the scheme (3.1) and the lower frame corresponds to the scheme (4.16). The various regions are as follows: *S*, the safe region for simulations; *F*, the patterns freeze into metastable states; *C*, the

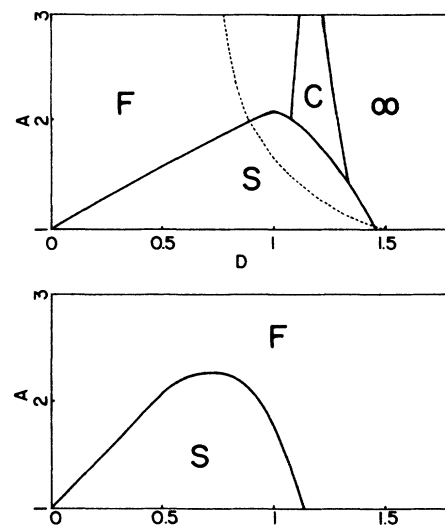


FIG. 21. Empirically obtained “safe” (denoted by *S*) regions of simulation for schemes (3.1) (upper frame) and (4.16) (lower frame), respectively. The behavior of the system in the various regions is explained in the text. A linear stability analysis suggests a “checkerboard” instability for parameter values to the right of the dotted line.

system goes into an unphysical, nonstationary checkerboard pattern (but without an arithmetic overflow);  $\infty$ , there is an arithmetic overflow in the simulation.

The regions  $C$  and  $\infty$  for the scheme (3.1) may qualitatively be understood as the result of a “checkerboard” instability in the bulk phase.<sup>12(c)</sup> If we linearize (3.1) about a stable fixed point of the tanh map (say,  $\psi_0$ ) we have

$$\delta(t+1, n) = \frac{A^2 - \psi_0^2}{A} \delta(t, n) + D [ \langle \langle \delta(t, n) \rangle \rangle - \delta(t, n) ], \tag{4.17}$$

where we have put  $\delta(t, n) = \psi(t, n) - \psi_0$ . Applying a discrete Fourier transform to both sides of this equation yields

$$\delta(t+1, k) = \frac{A^2 - \psi_0^2}{A} \delta(t, k) + D \left[ \frac{\cos k_x + \cos k_y + \cos k_x \cos k_y}{3} - 1 \right] \delta(t, k). \tag{4.18}$$

The maximum danger to the bulk stability is presented by the “checkerboard” fluctuation, where the fluctuation at a point is opposite to that of its nearest neighbors, with wave vector  $\mathbf{k} = (\pi, \pi)$ . This fluctuation grows when

$$-1 > \frac{A^2 - \psi_0^2}{A} - \frac{4D}{3}, \tag{4.19}$$

or

$$D > \frac{3}{4} + \frac{3}{4} \frac{A^2 - \psi_0^2}{A}. \tag{4.20}$$

This region corresponds to the right of the dotted line in the upper frame of Fig. 21. Notice that there are points in  $S$  which lie to the right of the dotted line also. These parameter values are linearly unstable, but the growing fluctuations are stabilized by the nonlinear term. Of course, it is a different question as to whether or not nonlinear stability is sufficient to give realistic results. The scheme (4.16) does not have the problem of arithmetic overflow because the solutions are bounded for all time. This follows from Proposition 2, which is proved shortly.

For  $D < 1$ , which is the region of interest to us, the scheme (4.16) has an expanded [over scheme (3.1)] range of parameter values where freezing does not occur. In Fig. 22 we show the evolution pattern for a  $100 \times 100$  lattice with  $A = 1.9$  and  $D = 0.5$ , using the scheme (4.16). This set of parameters would have given rise to a frozen pattern for the scheme (2.7), due to much harder phase-boundary walls and to an oscillatory local dynamics for (4.14). Notice that even parameter values (e.g.,  $A = 2.1$ ,  $D = 0.7$ ) which give chaotic local dynamics for (4.14) are in the safe region. The “safe” region for simulations of (3.2) and the conserved analog of (4.16) lies within the safe region for the corresponding nonconserved cases. We should emphasize that the behavior indicated in the various regions of Fig. 21 holds only for a majority, and not all, of the initial conditions we considered; there are certain initial conditions which give rise to behavior other than that which may be expected on the basis of the parameter value for the simulation. We believe that the study of numerical schemes which are not always reliable but work for a majority of cases is practically important. This is quite parallel to the study of approximate algorithms.

The scheme (4.15) has a theoretical (and maybe practi-

cal) advantage over the scheme we have been using: for moderate values of diffusion we can explicitly show a comparison theorem for the scheme (4.15). This theorem is one of the keys to many assertions about the qualitative features of the solution to a numerical scheme. The stability (i.e., the boundedness of the solution for any  $t > 0$ ) follows if we impose some additional conditions (which are usually satisfied) to the comparison theorem.

*Proposition 2 (comparison theorem).* Given any two initial conditions  $\{\psi_1(0, n)\}$  and  $\{\psi_2(0, n)\}$ , such that  $\psi_1(0, n) \geq \psi_2(0, n)$  for all  $n$ , then the corresponding solutions to (4.15) satisfy  $\psi_1(t, n) \geq \psi_2(t, n)$  for all  $t > 0$  and  $n$ , if (1)  $0 \leq \gamma \leq \frac{1}{2}$  and (2) the solution semigroup  $F_{\Delta t}$  is monotonically increasing.

*Proof.* Let  $\{\psi_1(t, n)\}(\{\psi_2(t, n)\})$  be the solution to (4.15) with the initial conditions  $\{\psi_1(0, n)\}(\{\psi_2(0, n)\})$ . Suppose that  $\psi_1(t, n) \geq \psi_2(t, n)$  for all  $n$ . Then

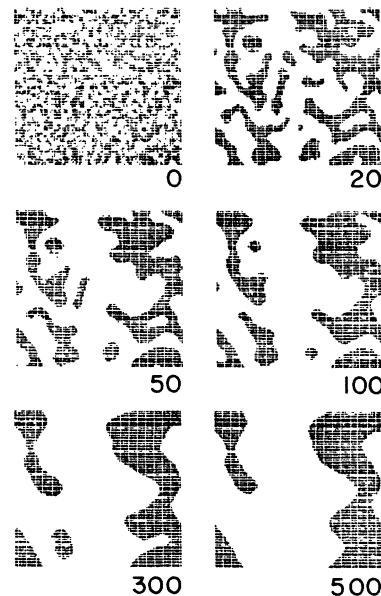


FIG. 22. Evolution patterns for the nonconserved case using the scheme (4.16) with the same initial condition as in Fig. 3, etc. The parameter values used for this evolution (i.e.,  $A = 1.9$ ,  $D = 0.5$ ) give rise to frozen patterns for the scheme (3.1) and to an oscillatory local dynamics for the Euler scheme.

$$\psi_1(t + \Delta t, n) - \psi_2(t + \Delta t, n) = (1 - 2\gamma)[F_{\Delta t}(\psi_1(t, n)) - F_{\Delta t}(\psi_2(t, n))] + 2\gamma[\langle\langle F_{\Delta t}(\psi_1(t, n)) \rangle\rangle - \langle\langle F_{\Delta t}(\psi_2(t, n)) \rangle\rangle]. \quad (4.21)$$

Since  $F_{\Delta t}$  is monotonically increasing,  $F_{\Delta t}(\psi_1(t, n)) \geq F_{\Delta t}(\psi_2(t, n))$  for all  $n$ . Hence, as long as  $0 \leq \gamma \leq \frac{1}{2}$ , we have  $\psi_1(t + \Delta t, n) \geq \psi_2(t + \Delta t, n)$ . By assumption,  $\psi_1(0, n) \geq \psi_2(0, n)$  for all  $n$ , so that  $\psi_1(t, n) \geq \psi_2(t, n)$  for all  $t > 0$  and  $n$ .

If we require, further, that the solution semigroup  $F_{\Delta t}$  have real numbers  $\alpha$  and  $\beta$  ( $\alpha > \beta$ ) such that  $F_{\Delta t}(\alpha) \leq \alpha$  and  $F_{\Delta t}(\beta) \geq \beta$ , then we can easily prove the stability of the scheme (4.15) for initial configurations satisfying  $\alpha \geq \psi(0, n) \geq \beta$  for all  $n$ .

In the original scheme (4.5), neither Proposition 2 nor the stability proof holds in general. However, if the initial condition is close to the origin in the TDGL case,  $F_{\Delta t}(\psi) - \psi$  is, in general, larger than  $-\epsilon$  (where  $\epsilon$  is a small positive number), since overshooting beyond the stable fixed point is difficult. Hence, practically, the above proposition is applicable. Of course, stability of a scheme does not imply accuracy or even qualitative reliability. Nevertheless, it is a prerequisite for a qualitative analysis, e.g., the study of the number of peaks in the solution.<sup>25</sup>

A slightly different scheme is also possible. When we make the wall hard enough, the patterns often freeze into metastable states. The freezing is due to the relative ineffectiveness of the intercell coupling. Hence it is reasonable to take the intercell coupling term into account (in a mean-field way) for the calculation of the semigroup. This results in the following scheme:

$$\psi(t + \Delta t, n) = F_{\Delta t}(\psi(t, n) + 2\gamma[\langle\langle \psi(t, n) \rangle\rangle - \psi(t, n)]). \quad (4.22)$$

Again, for small  $\Delta t$ , it is easy to show the equivalence of this to the original scheme. We should point out that this scheme may be considered as being a step out of phase with scheme (4.15), which can be written as a two-step process,

$$\begin{aligned} \psi \left[ t + \frac{\Delta t}{2}, n \right] &= F_{\Delta t}(\psi(t, n)), \\ \psi(t + \Delta t, n) &= (1 - 2\gamma)\psi \left[ t + \frac{\Delta t}{2}, n \right] \\ &\quad + 2\gamma \left[ \langle\langle \psi \left[ t + \frac{\Delta t}{2}, n \right] \rangle\rangle \right]. \end{aligned} \quad (4.23)$$

However, in general, the schemes (4.15) and (4.22) give rise to different evolution patterns from the same initial condition. We do expect them to have the same range of nonfreezing values, though. The comparison theorem also holds for this scheme for  $0 \leq \gamma \leq \frac{1}{2}$ .

We believe that all these schemes are in the same universality class, at least for the study of phase-ordering kinetics. The advantage of schemes (4.15) and (4.22) over (3.1) lies in the fact that these can rapidly give rise to a hard-wall evolution without freezing. As we have argued briefly here [and explain in detail in part II (Ref. 11)], the

asymptotic regime is reached faster with a hard-wall evolution.

Although, empirically, our schemes do appear to be qualitatively reliable, we are unable to theoretically assert anything about their qualitative reliability, due mainly to two reasons: (1) the qualitative theory of partial differential equations is not yet highly developed,<sup>27</sup> and (2) we do not precisely know what we mean by “qualitatively good.” However, there are mathematical results which will be useful in qualitative numerical analysis. They are almost all on the subject of semilinear parabolic equations. The work of Tabata<sup>25</sup> discusses a finite-different scheme which preserves the number of peaks in the solution to semilinear parabolic equations. The paper by Weinberger<sup>28</sup> already captures the spirit of qualitative numerical analysis. Mimura’s paper<sup>29</sup> clearly discusses the problem of numerical analysis of asymptotic behaviors.

## V. DISCUSSION AND SUMMARY

This paper is part I of an exposition of a cell-dynamical-system approach to phase-ordering dynamics. Part I is mainly devoted to methodological questions. It should, however, be apparent that our approach is sufficiently realistic and powerful. This conclusion will be amply demonstrated in part II (Ref. 11).

As we have stated in the Introduction, our fundamental approach toward analytical models is determined by the following observation: *Nature gives us phenomena, not equations*. Consequently, there is nothing sacrosanct about conventional continuum models. We have introduced discrete space-time models which can be constructed without invoking the corresponding partial-differential-equation description. This elementary construction of CDS models is generally easy to apply.

Historically, however, it is true that the first attempts at modeling various phenomena have been in terms of partial differential equations. Thus, it would be nice to have a systematic method of deriving efficient CDS models from the corresponding differential equation. In this paper we have proposed a new discretization scheme which gives rise to efficient CDS models for the class of semilinear parabolic equations. Furthermore, we emphasize that since there is no fundamentally justifiable way to derive partial-differential-equation models from a “microscopic reality,” there is no deep meaning in solving analytical models precisely. Rather, we need solve them only qualitatively. This leads us to request that the attention of applied mathematicians be directed towards a discipline that could be termed *qualitative numerical analysis*. Although such a discipline is a desirable goal, at present there may exist many technical and conceptual difficulties.

An example of modeling along the lines of this paper is provided by the modeling of phase-separation dynamics in block copolymer systems.<sup>30</sup> A recent CDS modeling of tricritical systems by Ohta *et al.*,<sup>31</sup> which seems to be

reasonably successful, should be justified from this point of view also.

Reversing the procedure above, we can construct partial-differential-equation models from CDS models in cases where the CDS models are easier to construct. A good example is that of block copolymer systems,<sup>30</sup> where the CDS models have motivated a new class of partial-differential-equation models,

$$\frac{\partial \psi(\mathbf{r}, t)}{\partial t} = L \nabla^2 \frac{\delta H[\psi(\mathbf{r}, t)]}{\delta \psi(\mathbf{r}, t)} - b \psi, \quad (5.1)$$

where  $b$  is a positive parameter and other symbols have the same meaning as previously. The innocent-looking modification (the term  $-b\psi$ ) of the Cahn-Hilliard equation drastically changes its behavior; nonuniform (e.g., striped) patterns become stationary solutions. Another example is motivated by our observation in Sec. II C about the free-energy functional which can be associated with the map  $f_2$ . Replacing this functional in the Cahn-Hilliard equation gives (after suitable rescaling)

$$\frac{\partial \psi(\mathbf{r}, t)}{\partial t} = \begin{cases} -\nabla^2 \psi(\mathbf{r}, t) - \nabla^4 \psi(\mathbf{r}, t) & \text{for } |\psi| \leq \psi_c \\ -\nabla^4 \psi(\mathbf{r}, t) & \text{for } |\psi| > \psi_c, \end{cases} \quad (5.2)$$

where  $\psi_c$  is a positive constant. We expect that this piecewise linear partial differential equation describes spinodal decomposition as a  $C^2$  solution to (5.2).

We may summarize our assertions as follows: we want to describe macroscopic phenomenological behavior of phase ordering essentially free of microscopic details. We call the totality of successful models which describe the

features of a set of macroscopic behaviors the universality class of models belonging to the set. The idea is parallel to the one used in the renormalization-group approach. We assert that each such class contains not only partial-differential-equation models but also our CDS models. We have qualitatively demonstrated in this paper that our CDS models capture the salient features of phase-ordering dynamics; the demonstration in part II (Ref. 11) will be much more extensive and quantitative. We believe that there are vast possibilities for studying nonlinear phenomena using CDS models. For example, introducing a complex-order-parameter CDS system, we can study coupled rotator systems<sup>32</sup> or phase transitions in the  $q$ -state Potts model.<sup>33</sup> Furthermore, by choosing asymmetric maps, we can study, e.g., liquid-gas phase transitions or polymer-solvent systems. Many of these are currently being studied by our group.

#### ACKNOWLEDGMENTS

We are grateful to T. Ohta, N. Goldenfeld, M. Yamaguti, F. Albrecht, and Y. Shiwa for many useful discussions and comments. We especially benefited from T. Ohta's lectures. A special thanks is due to N. Goldenfeld, who insisted that we should find a relation between the partial-differential-equation approach and our approach. We are grateful to M. Salamon for his interest in the generous support of our project. Our simulation was facilitated by V. Metze. This work was, in part, supported by National Science Foundation Grant No. DMR-84-15063 through the Materials Research Laboratories Program.

<sup>1</sup>For recent reviews, see J. D. Gunton, M. San Miguel, and P. S. Saint, in *Phase Transitions and Critical Phenomena*, edited by C. Domb and J. L. Lebowitz (Academic, New York, 1983), Vol. 8; J. L. Lebowitz, J. Marro, and M. H. Kalos, *Comments Solid State Phys.* **10**, 201 (1983); H. Furukawa, *Adv. Phys.* **34**, 703 (1985); K. Binder, in *Statistical Physics*, edited by H. E. Stanley (North-Holland, Amsterdam, 1986); J. D. Gunton (unpublished).

<sup>2</sup>J. W. Cahn and J. E. Hilliard, *J. Chem. Phys.* **28**, 258 (1958); **31**, 688 (1959); H. E. Cook, *Acta Metall.* **18**, 297 (1970).

<sup>3</sup>(a) K. Binder and D. Stauffer, *Phys. Rev. Lett.* **33**, 1006 (1974); (b) H. Furukawa, *Phys. Lett.* **62A**, 377 (1977); *Prog. Theor. Phys.* **59**, 1072 (1978); *Phys. Rev. Lett.* **43**, 136 (1979).

<sup>4</sup>(a) K. Kawasaki and T. Ohta, *Prog. Theor. Phys.* **67**, 147 (1982); **68**, 129 (1982); (b) K. Kawasaki, Y. Enomoto, and M. Tokuyama, *Physica A* **135**, 426 (1986); M. Tokuyama, Y. Enomoto, and K. Kawasaki, *ibid.* **143**, 183 (1987); (c) T. Ohta, *Prog. Theor. Phys. Suppl.* **71**, 1409 (1984); *Ann. Phys.* **158**, 31 (1984).

<sup>5</sup>J. S. Langer, M. Bar-On, and H. P. Miller, *Phys. Rev. A* **11**, 1417 (1975).

<sup>6</sup>E. D. Siggia, *Phys. Rev. A* **20**, 595 (1979); K. Kawasaki and T. Ohta, *Prog. Theor. Phys.* **67**, 147 (1982); *Physica A* **118**, 175 (1983).

<sup>7</sup>For nonconserved-order-parameter-case Monte Carlo results, see M. K. Phani, J. L. Lebowitz, M. H. Kalos, and O. Penrose, *Phys. Rev. Lett.* **45**, 366 (1980); P. S. Sahni, G. Dee, J. D. Gunton, M. Phani, J. L. Lebowitz, and M. H. Kalos, *Phys. Rev. B* **24**, 410 (1981).

<sup>8</sup>For conserved-order-parameter-case Monte Carlo results, see J. Marro, J. L. Lebowitz, and M. H. Kalos, *Phys. Rev. Lett.* **43**, 282 (1979); O. Penrose, J. L. Lebowitz, J. Marro, M. H. Kalos, and A. Sur, *J. Stat. Phys.* **19**, 243 (1978); J. L. Lebowitz, J. Marro, and M. H. Kalos, *Acta Metall.* **30**, 297 (1982); P. S. Sahni and J. D. Gunton, *Phys. Rev. Lett.* **45**, 369 (1980); E. T. Gawlinski, M. Grant, J. D. Gunton, and K. K. Kaski, *Phys. Rev. B* **31**, 281 (1985).

<sup>9</sup>(a) G. F. Mazenko, O. T. Valls, and F. C. Zhang, *Phys. Rev. B* **32**, 5807 (1985); G. F. Mazenko and O. T. Valls, *Phys. Rev. Lett.* **59**, 680 (1987); (b) D. Huse, *Phys. Rev. B* **34**, 7845 (1986).

<sup>10</sup>R. Petschek and H. Metiu, *J. Chem. Phys.* **79**, 3443 (1985); T. Miyazaki, T. Kozakai, S. Mizuno, and M. Doi, *Trans. Jpn. Inst. Met.* **24**, 799 (1983).

<sup>11</sup>S. Puri and Y. Oono, *Phys. Rev. A* (to be published).

<sup>12</sup>(a) For example, see S. Wolfram, *Theory and Applications of Cellular Automata* (World Scientific, Singapore, 1986); J. Demongeot, E. Cole, and M. Tchuente, *Dynamical Systems and Cellular Automata* (Academic, New York, 1985); (b) K. Kaneko, *Prog. Theor. Phys.* **72**, 480 (1984); R. J. Deissler, *Phys. Lett.* **100A**, 451 (1984); R. Kapral, *Phys. Rev. A* **32**, 1076 (1985); (c) G. L. Oppo and R. Kapral, *ibid.* **33**, 4219 (1986); R. Kapral and G. L. Oppo, *Physica D* **23**, 455 (1986); G. L. Oppo and R. Kapral (unpublished).

<sup>13</sup>(a) U. Frisch, B. Hasslacher, and Y. Pomeau, *Phys. Rev. Lett.* **56**, 1505 (1986); S. Orszag and V. Yakhot, *ibid.* **56**, 1691 (1986); (b) H. Chen and W. H. Matthaeus, *ibid.* **58**, 1845 (1987).

- <sup>14</sup>(a) M. Creutz, *Ann. Phys.* **167**, 62 (1986); R. Shaw (private communication); (b) N. Packard, in *Proceedings of the First International Symposium on Growth and Form, Tsukuba, 1985*, edited by Y. Katoh, R. Takaki, J. Toriwaki, and S. Ishizaka (KTK Scientific, 1986).
- <sup>15</sup>(a) J. Greenberg, C. Green, and S. Hastings, *SIAM (Soc. Ind. Appl. Math.) J. Algebraic Discrete Methods* **1**, 34 (1980); B. F. Madore and W. L. Freedman, *Science* **222**, 615 (1983); D. A. Young, *Math. Biosci.* **72**, 51 (1984); (b) Y. Oono and M. Kohmoto, *Phys. Rev. Lett.* **55**, 2927 (1985); Y. Oono and C. Yeung, *J. Stat. Phys.* **48**, 593 (1987).
- <sup>16</sup>B. I. Halperin and P. C. Hohenberg, *Rev. Mod. Phys.* **49**, 435 (1977).
- <sup>17</sup>For example, see K. G. Wilson and J. Kogut, *Phys. Rep.* **12**, 76 (1974).
- <sup>18</sup>(a) From a summary, see J. L. Lebowitz, *Physica A* **140**, 232 (1986); (b) K. Kitahara and M. Imada, *Prog. Theor. Phys. Suppl.* **64**, 65 (1978).
- <sup>19</sup>Y. Oono and S. Puri, *Phys. Rev. Lett.* **58**, 836 (1987).
- <sup>20</sup>T. Ohta, D. Jasnow, and K. Kawasaki, *Phys. Rev. Lett.* **49**, 1223 (1982); T. Ohta (private communication).
- <sup>21</sup>Y. Oono, S. Puri, C. Yeung, and M. Bahiana, *J. Appl. Crystallogr.* (to be published); S. Puri and Y. Oono (unpublished).
- <sup>22</sup>M. Shub, *Global Stability of Dynamical Systems* (Springer-Verlag, New York, 1987).
- <sup>23</sup>G. Porod, in *Small Angle X-Ray Scattering*, edited by O. Glatter and L. Kratky (Academic, New York, 1983).
- <sup>24</sup>M. Yamaguti and H. Hatano, *Proc. Jpn. Acad. Sci., Ser. A* **55**, 78 (1979).
- <sup>25</sup>M. Tabata, *J. Math. Soc. Jpn.* **32**, 191 (1986); in *Numerical Analysis and Nonlinear Phenomena* (in Japanese), edited by M. Yamaguti (Nihonhyoronsha, Tokyo, 1981).
- <sup>26</sup>(a) M. Mizutani, J. Niwa, and T. Ohno, *J. Math. Kyoto Univ.* **23**, 39 (1983); (b) J. B. Kogut, *Rev. Mod. Phys.* **55**, 775 (1983).
- <sup>27</sup>For a useful summary, see J. K. Hale, in *Nonlinear Difference Equations*, edited by J. K. Hale and D. Martinez-Amores (Pitman, Boston, 1985).
- <sup>28</sup>H. F. Weinberger, *SIAM (Soc. Ind. Appl. Math.) J. Math. Anal.* **13** 353 (1982).
- <sup>29</sup>M. Mimura, in *Numerical Analysis and Nonlinear Phenomena* (in Japanese), edited by M. Yamaguti (Nihonhyoronsha, Tokyo, 1981).
- <sup>30</sup>Y. Oono and Y. Shiwa, *Mod. Phys. Lett. B* **1**, 49 (1987).
- <sup>31</sup>T. Ohta, K. Kawasaki, A. Sato, and Y. Enomoto (unpublished).
- <sup>32</sup>Y. Kuramoto, *Prog. Theor. Phys. Suppl.* **79**, 223 (1984); Y. Kuramoto and I. Nishikawa (unpublished).
- <sup>33</sup>P. S. Sahní, D. J. Srolovitz, G. S. Grest, M. P. Anderson, and S. A. Safran, *Phys. Rev. A* **28**, 2705 (1984); S. Kumar, J. D. Gunton, and K. K. Kaski, *Phys. Rev. B* **35**, 8517 (1987).

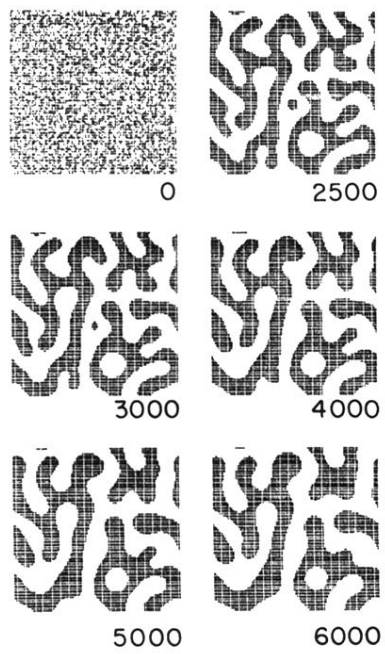


FIG. 10. Long-time evolution patterns for the conserved case using the tanh map. The random initial configuration is the same as that used previously.

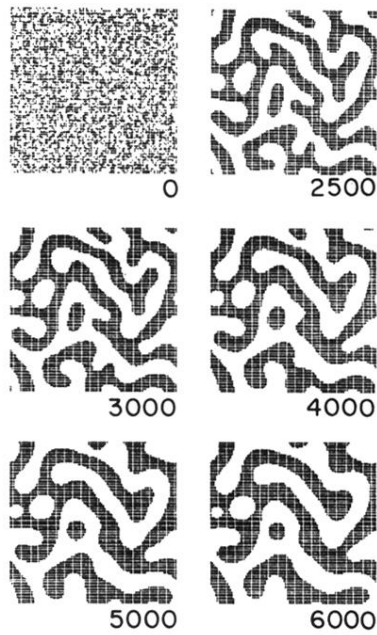


FIG. 12. Long-time evolution patterns for the conserved case with a soft-wall evolution. Again, we use the same initial condition as previously.

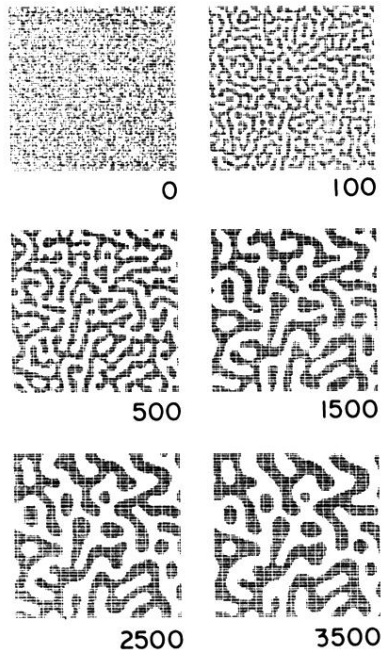


FIG. 14. Long-time evolution patterns for the conserved case with naively discretized Laplacian, i.e.,  $\langle\langle \psi(t, n) \rangle\rangle$  defined by (3.3). The initial condition is the same as before. The pattern at time 3500 should be compared with the pattern at time 2500 in Fig. 12, as the smaller value of  $D$  gives a considerably slower evolution in this case. Comparing these patterns, we see that the pattern at time 3500 has a tendency to be preferentially inclined along the [10] and [01] directions.

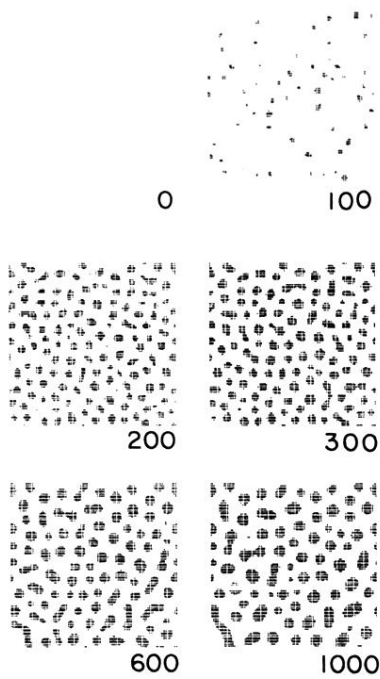


FIG. 15. Evolution patterns for the conserved case with an off-critical quench. The random initial configuration has the order parameter uniformly distributed between  $-0.3 \pm 0.125$ . Clustering, necking, and cluster evaporation are evident in the later stages.

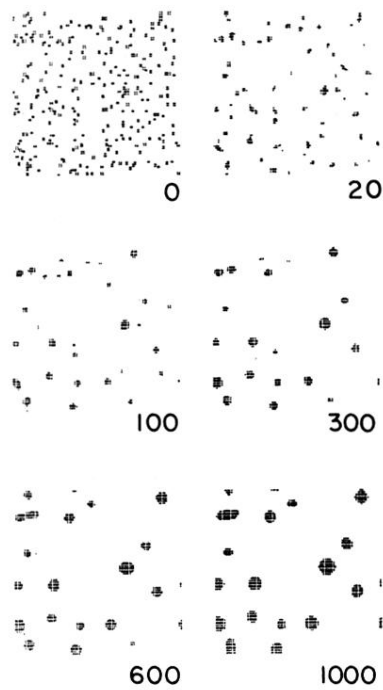


FIG. 17. Evolution patterns for the conserved case in the nucleation regime. The random initial configuration is constructed by having the order parameter uniformly distributed between  $-0.6 \pm 0.125$  with randomly placed seeds (each consisting of at least four sites each and adding up to about 10% of the lattice) of order parameter  $+0.98$ . The sites with negative order parameter are then biased so that the average order parameter at each site is  $-0.6$ , corresponding to a minority species concentration of 20%.

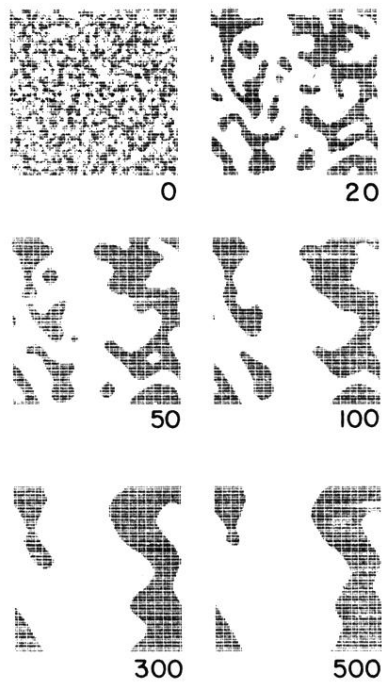


FIG. 20. Evolution patterns for the nonconserved case using the scheme (4.16) with the same initial condition as in Fig. 3, etc.

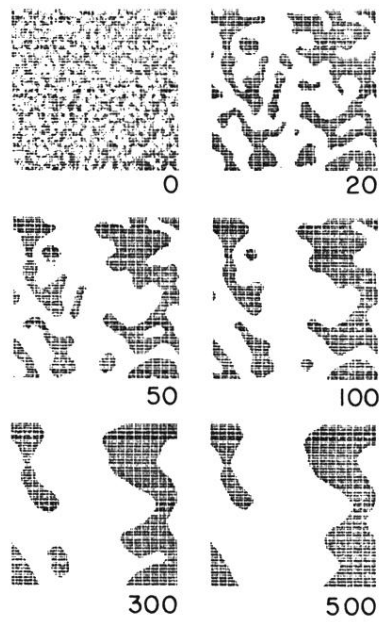


FIG. 22. Evolution patterns for the nonconserved case using the scheme (4.16) with the same initial condition as in Fig. 3, etc. The parameter values used for this evolution (i.e.,  $A=1.9$ ,  $D=0.5$ ) give rise to frozen patterns for the scheme (3.1) and to an oscillatory local dynamics for the Euler scheme.

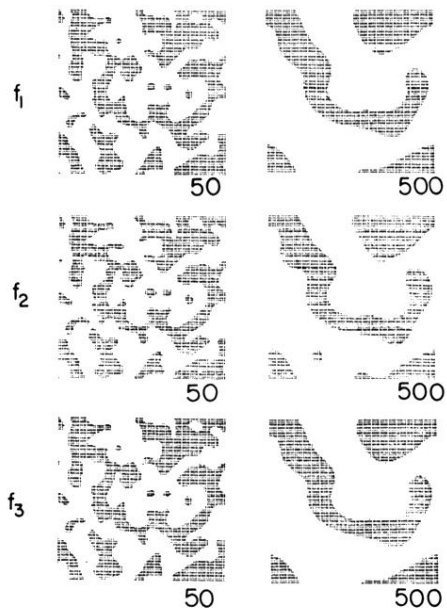


FIG. 3. Evolution patterns for the nonconserved case using maps  $f_1$ ,  $f_2$ , and  $f_3$  from the same random initial configuration. The top two pictures are for the map  $f_1$ , the middle two are for the map  $f_2$ , and the bottom two are for the map  $f_3$ . The numbers denote necessary time steps from the initial condition. Only points with positive order parameters are marked. This coding is also used in all subsequent evolution patterns we display in this paper.

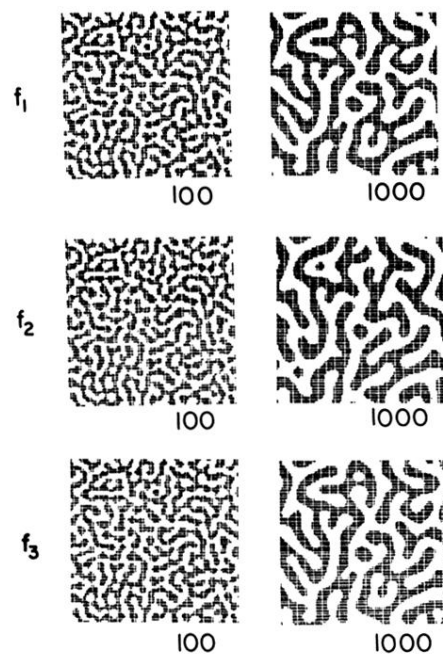


FIG. 4. Evolution patterns for the conserved case using maps  $f_1$ ,  $f_2$ , and  $f_3$  from the same random initial configuration as in Fig. 3.

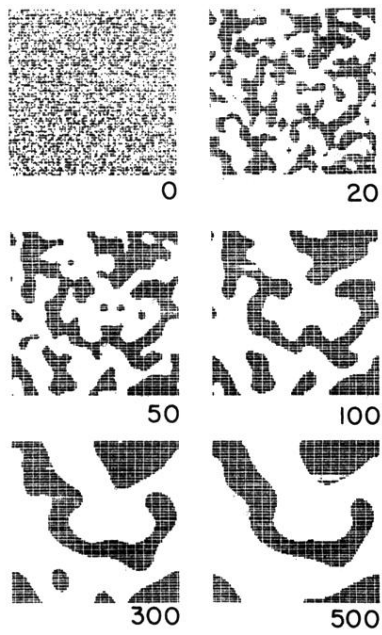


FIG. 8. Long-time evolution patterns for the nonconserved case using the tanh map ( $f_1$ ). The random initial configuration is the same as that used previously and is labeled by 0 in the figure.